Bioactive Materials 26 (2023) 216–230

Contents lists available at ScienceDirect

Bioactive Materials

journal homepage: www.keaipublishing.com/en/journals/bioactive-materials

Creating a semi-opened micro-cavity ovary through sacrificial microspheres as an *in vitro* model for discovering the potential effect of ovarian toxic agents

Min Ye [a,b,c], Yiran Shan [d], Bingchuan Lu [a,b,c], Hao Luo [a,b,c], Binhan Li [a,b,c], Yanmei Zhang [a,b,c], Zixuan Wang [a,b,c], Yuzhi Guo [a,b,c], Liliang Ouyang [a,b,c], Jin Gu [d], Zhuo Xiong [a,b,c,**], Ting Zhang [a,b,c,*]

[a] *Biomanufacturing Center, Department of Mechanical Engineering, Tsinghua University, Beijing, 100084, China*
[b] *Biomanufacturing and Rapid Forming Technology Key Laboratory of Beijing, Beijing, 100084, China*
[c] *Biomanufacturing and Engineering Living Systems, Innovation International Talents Base (111 Base), Beijing, 100084, China*
[d] *MOE Key Laboratory of Bioinformatics, BNRIST Bioinformatics Division, Department of Automation, Tsinghua University, Beijing, 100084, China*

ARTICLE INFO

Keywords:
Bio-engineered ovary
SOCS
Semi-opened MCO
Ovarian model
Drug study

ABSTRACT

The bio-engineered ovary is an essential technology for treating female infertility. Especially the development of relevant *in vitro* models could be a critical step in a drug study. Herein, we develop a semi-opened culturing system (SOCS) strategy that maintains a 3D structure of follicles during the culture. Based on the SOCS, we further developed micro-cavity ovary (MCO) with mouse follicles by the microsphere-templated technique, where sacrificial gelatin microspheres were mixed with photo-crosslinkable gelatin methacryloyl (GelMA) to engineer a micro-cavity niche for follicle growth. The semi-opened MCO could support the follicle growing to the antral stage, secreting hormones, and ovulating cumulus-oocyte complex out of the MCO without extra manipulation. The MCO-ovulated oocyte exhibits a highly similar transcriptome to the *in vivo* counterpart (correlation of 0.97) and can be fertilized. Moreover, we found that a high ROS level could affect the cumulus expansion, which may result in anovulation disorder. The damage could be rescued by melatonin, but the end of cumulus expansion was 3h earlier than anticipation, validating that MCO has the potential for investigating ovarian toxic agents *in vitro*. We provide a novel approach for building an *in vitro* ovarian model to recapitulate ovarian functions and test chemical toxicity, suggesting it has the potential for clinical research in the future.

1. Introduction

The ovary consists of the cortex, medulla, and hilum regions [1], which is one of the major organs responding to reproductive behaviors, such as generating female hormones and gametes. In the mammalian ovary, primary follicles develop to form secondary follicles, in which oocytes are surrounded by two or more granulosa cells (GCs) layers. An antrum is formed and filled with follicular fluid as the follicle grows. The GCs are separated into two functional cell types, the mural GC, responsible for steroidogenesis, and the cumulus cells, which are adjacent to the oocyte [2,3]. Then, the oocyte is ruptured out of the ovary, which is stimulated by the LH surge [4,5]. Currently, nearly 15% of reproductive-aged couples face infertility. Therefore, the effect of ovarian drugs and agents is needed to be assessed for treating infertility. Recently, the use of specialized *in vitro* ovarian models has also been highlighted in identifying toxicology for specific drugs or chemicals. Compared to *in vivo* animal models, which might not represent the human body and are hard to trace the cellular response in real-time due to limitations of *in vivo* imaging techniques, the *in vitro* model can provide much more reliable test results. Thus, developing relevant *in vitro* models could be a critical step in drug discovery. The previous bio-engineered ovary was mainly fabricated based on a 3D culture system, where the follicle was encapsulated in the hydrogel. Although such a 3D culture system could retain intracellular communication [6,7],

Peer review under responsibility of KeAi Communications Co., Ltd.
* Corresponding author. Biomanufacturing Center, Department of Mechanical Engineering, Tsinghua University, Beijing, 100084, China.
** Corresponding author. Biomanufacturing Center, Department of Mechanical Engineering, Tsinghua University, Beijing, 100084, China.
E-mail addresses: xiongzhuo@tsinghua.edu.cn (Z. Xiong), t-zhang@mail.tsinghua.edu.cn (T. Zhang).

https://doi.org/10.1016/j.bioactmat.2023.02.029
Received 30 November 2022; Received in revised form 26 February 2023; Accepted 26 February 2023

whereas the 2D culture system cannot [6], the dynamic follicular process has not been fully recovered. For example, the ovulated oocyte, which is spontaneously extruded from the ovary *in vivo* [8], is usually obtained with mechanical/enzyme isolation or relies on the self-degradation of hydrogel, which is uncontrollable and variant in batches.

Bio-manufacturing is a promising technique that can construct bio-engineered tissues with fine-tuned microstructures and mechanical properties, which may help mimic the dynamic development process *in vivo*. Many bio-manufacturing methods, including the mold approach, microfluidic technology, electrospinning, and 3D printing, are well-utilized in tissue engineering [9–17]. These technologies aim to imitate the mechanics, components, and morphology of natural tissues. Pilot studies focused on using microfluidic systems to generate shape-controlled hydrogels [18], which have been used as the basic unit in additive manufacturing, such as 3D printing, cell culture, and drug delivery [19–23]. One emerging application is to generate sacrificial microparticles through microfluidic, a promising one-step strategy for creating cavities in a macroscopic construct [24–26]. Therefore, applying these technologies will increase the complexity of a bio-engineered ovary, which may enrich the function of the *in vitro* model. Many studies confirmed that the surrounding stiffness of follicles affects follicular development [27–31]. For example, follicles of different species have distinguished responses to similar physical conditions. A high modulus of the matrix may prohibit granulosa cell proliferation for murine preantral follicles while maintaining an intact primordial follicular morphology in primates. These findings suggest that the culturing environment should be optimized according to the ovarian physiological mechanics.

Many hydrogels, including Matrigel [32–34], collagen [35], calcium alginate matrix [28,33,34,36], hyaluronan [37], polyethylene glycol (PEG) [38], and decellularized matrix [39–41] have been used in follicle 3D culture. Among them, gelatin is a protein derived from collagen and found in many organ compositions and has been wildly used for tissue engineering [42,43]. In particular, gelatin methacrylate (GelMA) has gained increasing attention because of its transparent structure for cell monitoring, biocompatibility, biodegradability, and tunability in chemical and mechanical properties [44]. GelMA has been previously used in culturing vascular cells [45,46], cardiomyocytes [47], pluripotent cells [48], and germ cells [49], showing its broad biocompatibility in bio-manufacturing.

In this study, we developed a strategy (Fig. 1a) for a novel semi-

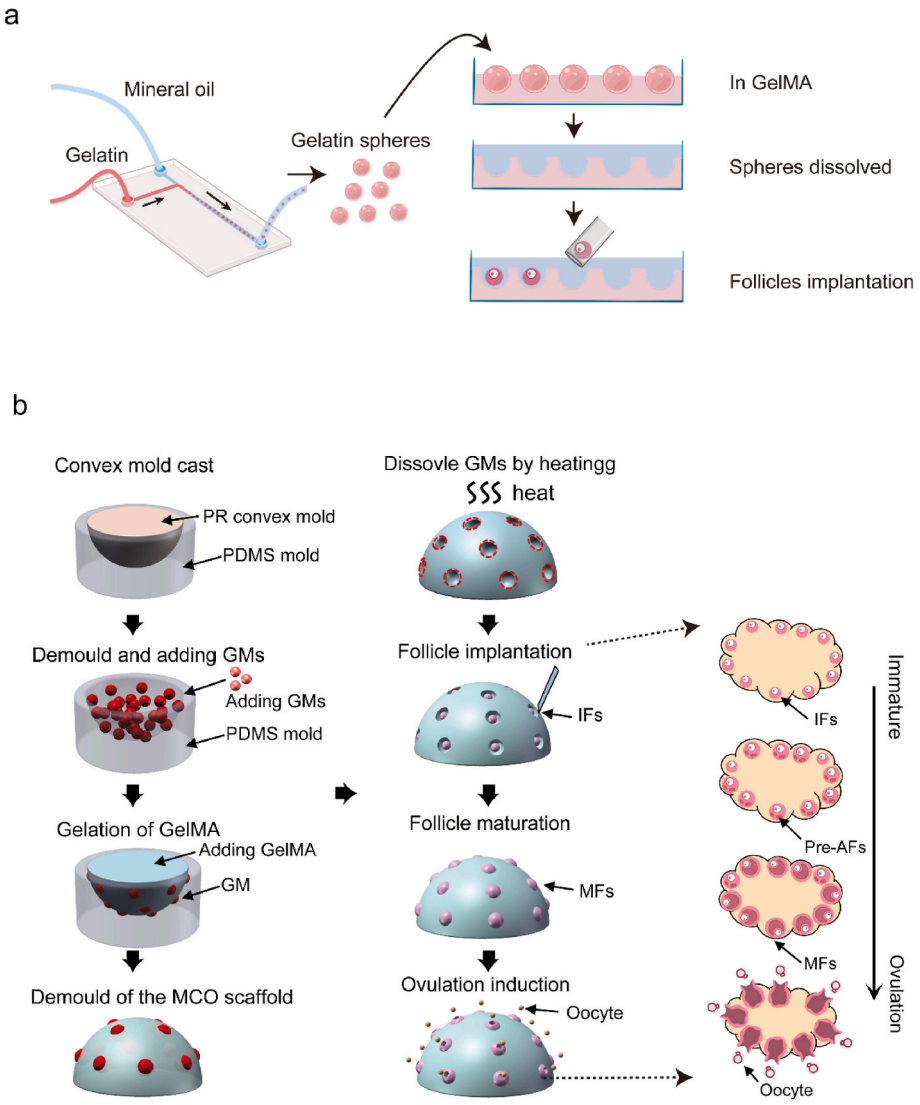

Fig. 1. The strategy of fabricating the semi-opened MCO. **a**. The fabrication scheme of the semi-opened culture system; **b**. The fabrication scheme of the MCO and the corresponding *in vivo* ovary stages. MCO: micro-cavity ovary; PR: photosensitive resin; GM: gelatin microsphere; IF: immature follicle; Pre-AF: pre-antral follicle; MF: matured follicle; MO: MII oocyte.

opened culture system (SOCS) for ovarian follicles using a microfluidic and molding approach with optimized GelMA parameters and sacrificial microspheres. The SOCS allows follicles to grow by maintaining a 3D structure. Based on this system, we further investigate a scheme to build a bio-engineered micro-cavity ovary (MCO) model (Fig. 1b). The MCO model undergoes various dynamic processes involved in follicular development, hormone secretion, and ovulation. Moreover, the MCO responds rapidly to the change in environmental chemicals, proving its potential to serve as a valuable tool for future tissue engineering and toxicological research.

2. Materials and methods

2.1. Fabrication of the T-shape microfluidic device and microspheres production

SYLGARD 184 silicone rubber kit (DOW) was used to make a T-shaped microfluidic chip. The two liquids were mixed in a beaker at a 10:1 ratio and stirred with a glass rod for at least 6 min. The mixed liquids were transferred to customized chip molds. Two steel needles were buried into the PDMS to form a T-shape channel. Then, the mixture was cross-linked in a drying oven at 45 °C overnight. Then, the cured T-shape microfluidic chip was de-molded (length: 25 mm, width: 15 mm, height: 10 mm). The diameter of the T-shape channel was restricted to the diameter of the needle, controlling the diameter of microspheres. Next, 7.5% w/v gelatin (Sigma, V900863) and oil phases (Sigma, M8410) with 2% v/v Span80 were pumped into the chip from the different sides with a velocity ratio of 1:5. The microsphere passed through an ice box to gelatinize the gelatin. Then, microspheres were collected in 15 ml centrifuge tubes and washed five times with pre-cooled PBS to replace the oil.

2.2. Synthesis of fluorescent gelatin

Rhodamine-conjugated gelatin can be obtained by reacting NHS-rhodamine (46406 Thermo Scientific) with gelatin. First, gelatin was fully dissolved in phosphate buffer (PH ≈ 8.1) at 50 °C to prepare a 10 wt % solution. After dissolving, NHS-rhodamine was added to the gelatin solution (30 mg of NHS-rhodamine for every gram of gelatin) and reacted for 3 h in the dark with stirring and heating (50 °C). Then the mixture was transferred to dialysis for 5–7 days with pure water at 40 °C, followed by freeze-drying and stored at −20 °C.

2.3. Collection of P16 mouse follicles

Animal use was performed under a Tsinghua University Institutional Animal Care and Use Committee (IACUC)-approved protocol with approval number (222) 368. P16 mouse follicles were collected from CD1 mice based on established protocol [50]. In brief, the P16 CD1 mouse was sacrificed, and the ovary was obtained and transferred to an L-15 medium (Sigma, L1518) with 5% FBS. The intact follicle was mechanically isolated.

2.4. In vitromaturation of P16 mouse follicles

The culture medium was prepared as the published protocol [51]. In brief, the maturation medium was composed of α-MEM (Gibco, 12571063) supplemented with 5% FBS, 0.1 IU/ml FSH (Sigma, F4021), 5 μg/ml insulin, 5 μg/ml transferrin, 5 ng/ml selenium (Sigma, 11074547001). The follicle was incubated at 37 °C, 5% CO_2 in the air. Half of the maturation medium was changed daily until the antral cavity was observed.

To induce ROS, 200 μm H_2O_2 was proved to be enough to induce cell damage [52,53] and applied to treat the follicle. To recover the ovulation process, follicles were pre-treated with 10 μm melatonin and performed ovulation induction with melatonin.

2.5. Ovulation induction and spontaneous parthenogenesis

The ovulation induction medium was composed of the maturation medium with 10–30 IU/ml chorionic gonadotropin for horses and 10 ng/ml mEGF (Peprotech, 315-09), incubating follicles at 37 °C, 5% CO^2 in the air for 16h ~ 18h. The oocyte spontaneously divided into a 2-cell stage within 24h of culture. The statistic value is mean ± SD.

2.6. Fabrication of the semi-opened MCO

The GelMA was bought from commercial products (EFL, EFL-GM-60 for GelMA60, EFL-GM-90 for GelMA90). The solution was prepared as 5%, 10%, 15% GelMA60, or GelMA90 with 0.25% LAP. The ovarian-like convex mold was designed by SolidWorks software. The size of the convex mold was 3 mm in diameter, ovarian-like shape. Then a concave PDMS mold was obtained by peeling it off the convex mold. Next, we poured gelatin microspheres and GelMA into the PDMS mold. Then the GelMA was crosslinked at 30 mW/cm^2 for the 30s to fabricate the MCO scaffold. After gel demolding, the MCO scaffold was incubated at 37 °C to dissolve microspheres. The immature follicle was mechanically dissociated. P16 immature follicles with healthy morphology were collected. Then, 20–30 isolated follicles were seeded to each MCO by narrow-tipped pipettes.

2.7. 3D culture of follicles with alginate and ovulation

The alginate droplet with 5–10 follicles was produced according to the published method [54,55] with some modifications. In brief, 0.5% (w/v) alginate was prepared with DPBS. Follicles were collected and re-suspended by the alginate solution. Then, 5–10 μl solution with follicles was dropped into 100 mM $CaCl_2$ for 2 min. The droplet was collected and washed by α-MEM twice, then cultured in maturation medium.

To release the follicles from the alginate hydrogel, the droplet was dissolved by 1% w/v sodium citrate in DPBS. Then the follicle was washed by α-MEM twice to remove the sodium citrate. Finally, the ovulation was induced by the ovulation induction medium.

2.8. Measurement of the diameter of follicles and the death/live ratio

The distance that divided the follicle into two symmetrical parts was measured. The distance must span the center of the oocyte. The death/live ratio was measured according to the intact morphology of follicles and oocytes (Fig. S1). The statistic value is mean ± SD.

2.9. Oocytes collection

GV oocytes were obtained from the P16 CD1 mouse ovary. In brief, the P16 CD1 mouse was sacrificed, and the ovary was removed to L-15 medium (Sigma, L1518) with 5% FBS. The secondary follicle was mechanically dissociated. Then, GV oocytes were released by puncturing the follicles with a 30 G sterile needle under a stereomicroscope. MII oocytes were collected from a 4-week CD1 mouse. Mice were injected with 10 IU pregnant mare serum gonadotropin (PMSG). Then, these mice were injected with 10 IU hCG 47h later. After 16h of the injection of hCG, the MII oocyte was collected. MCO oocytes were performed IVM as described in this study, and the matured oocytes with the first polar body were collected.

2.10. IVF procedure

The 8-week male mouse was sacrificed, and the epididymis was obtained. The epididymis was cut 3–4 times and transferred to HTF medium (Sigma, MR-070) to harvest matured sperms. After 1 h of sperm capacitation, sperms and oocytes were co-incubated for 4h ~ 6h at 37 °C, 5% CO_2 in the air. Then sperms were washed, and the fertilized

oocyte was transferred to the KOSM medium (Sigma, MR-101-D). The zygote was going to start cleavage within 12h.

2.11. Time-lapse record of the ovulation process

Follicles within the MCO were transferred into a 35 mm dish. Then, the dish was transferred into a NIKON TI2 live-cell workstation at 37 °C, 5% CO_2 in air for 24h. The ovulation process was recorded per 25min to form a time-lapse movie.

2.12. The elastic modulus test by AFM indentation

The ovary or GelMA was plated at the center of a 60 mm dish and soaked by DPBS (Hyclone, SH30028.01) at room temperature. The AFM used in our experiments is the MFP-3D™ Stand Alone AFM (Asylum Research) to align the probe to the samples optically. The probe we used was qp-SCONT (NanoAndMore) with a spring constant of 0.01 N/m. The cantilever applied the force mode with a predefined force of 1.5 nN. The cantilever was calibrated on the glass bottom before the measurements to determine the spring constant. At least three random locations in each sample were probed, and 36 points for each location were indented in an area of 20 × 20 μm. The elastic modulus was automatically calculated by ASYLUM RESEARCH software (Version 13.04.77), followed by the Oliver-Pharr formula. The distribution of the elastic modulus was fitted by the Gaussian curve. The statistic value is mean ± SD.

2.13. SEM image of the MCO

We froze the MCO scaffold at −80 °C overnight. Prior to the freeze-drying process, the freeze-dryer was pre-cooled. Then scaffolds were transferred to the freeze dryer before their thawing. The freeze-drying process was performed for 48h. The dried scaffold was mounted to carbon tape and coated with Pt with a Sputter Coater Leica EM ACE600. Images were scanned with a Hitachi S-5500 cold field emission scanning electron microscope.

2.14. SEM image of the ovary and the follicle within the MCO

The cell sample was fixed with 4% PFA (leagene, DF0133) in DPBS for 30 min. Then we prepared a series of ethanol solutions with 10%, 20%, 30%, 40%, 50%, 60%, 70%, 80%, 90%, and 100% concentrations. Then, the fixed cell sample was soaked in the ethanol solution from a low to a high concentration for 30 min each. Then the cell sample was dried in air overnight. The dried sample was mounted to carbon tape and coated with Pt using a Sputter Coater Leica EM ACE600. Images were scanned with a Hitachi S-5500 cold field emission scanning electron microscope.

2.15. Immunofluorescence staining of follicles within MCO

Follicles within the MCO were fixed by 4% PFA in DPBS for 30 min. Then the fixed cell was washed by 1 × TBST for 5 min twice. Then the sample was soaked in a blocking buffer composed of 1 × TBST with 10% donkey serum and 0.1% Triton-X for 1h. Preparing *anti*-Dazl (BIO-RAD, MCA2336) and *anti*-Amh (Abcam, ab272221) antibodies at 1 : 100 in blocking buffer and incubating the cell sample at 4 °C overnight. Antibodies were washed for 15 min three times, then Goat anti-Mouse Alexa Fluor™ Plus 488 antibody (A-11001) and Goat anti-Rabbit Alexa Fluor™ Plus 594 antibody (A-11012) were diluted at 1 : 300–1 : 500 ratio by blocking buffer. The cell sample was incubated in the secondary antibody buffer at room temperature for 1h–3h. Then the cell sample was washed for 15 min three times by 1 × TBST. The cell nuclear was stained by DAPI at 1 : 100 ratio for 30 min and washed. The data was obtained by NIKON A1 HD25 confocal microscope.

2.16. Characterization of meiotic oocyte

The ovulated oocyte was fixed by 4% PFA in DPBS with 0.1% Triton-X 100 at 37 °C for 1h. Then oocytes were washed three times by blocking buffer containing 1 × TBST (leagene, PW0020) with 0.3% BSA (Sigma, A1933). Next, oocytes were incubated in a blocking buffer with 1 : 50 dilution of *anti*-α-tubulin (Cell Signaling Technology, 5063S) at 4 °C overnight. The *anti*-α-tubulin was washed three times by blocking buffer and stained with DAPI of 1 : 100 dilution. The image was obtained by NIKON A1 HD25 confocal microscope.

2.17. Histological analysis of folliculogenesis

Follicles within the MCO were fixed by 4% PFA in DPBS for 30 min. Then the scaffold was washed by DPBS twice. 2% Gelatin and 2% agar solution were prepared in water, then the scaffold with follicles was encapsulated. After gelation, the scaffold was dissociated from the gel, then sequentially dehydrated by gradient ethanol, embedded in paraffin, and sectioned at 5 μm. The section slide was stained with hematoxylin and eosin and visualized by an Olympus IX73 microscope.

2.18. Hormone ELISAs

Mouse estradiol (Cayman, 501890), Inhibin-A (CUSABIO, CSB-E08238 M), and Inhibin-B (CUSABIO, CSB-E08151 m) hormones were tested by the corresponding ELISA kit. In brief, the supernatant of the culture medium was collected and diluted in a proper concentration to match the dynamic range of each ELISA kit. Each sample of ELISA was performed in duplicate, as at least three independent experiments. 50 μl of each sample was incubated in the ELISA plate at 37 °C for 1h, then washed three times. The ELISA-based color reaction was performed, and the ELISA plate was read at 450 nm by Thermo Multiskan Skyhigh optical reader to measure the concentration of each sample. The statistic value is mean ± SD.

2.19. Single-cell RNA-seq pre-processing

GV, SO-MII, and MOC-MII oocytes were obtained, who used the Smart-Seq2 protocol to prepare the RNA-seq libraries with a few modifications [56–58]. First, the zona pellucida was removed by Tyrode's solution (Sigma, T1788). Then, the naked oocyte was digested in 2.55ul cell lysis buffer containing RNase inhibitor (40 U/μL, TaKaRa, 2313A), Triton X-100 solution (10%, Sigma, 9036-19-5), Barcode primer (5 μM), and dNTP mix (10 mM, TaKaRa, 4019). The reverse transcription reaction was performed with 25 nt oligo (dT) primer anchored with an 8 nt cell-specific barcode and 8 nt unique molecular identifiers (UMIs) [59–61]. After the first-strand synthesis, the second-strand cDNAs were synthesized, and the cDNAs were amplified by 10–16 cycles of PCR (95 °C for 3 min, then 4 cycles of: 98 °C for 20 s, 65 °C for 30 s, and 72 °C for 5 min, followed by 10–16 cycles at 98 °C for 20 s, 67 °C for 15 s, and 72 °C for 5 min, with a final cycle at 72 °C for 5 min). The amplified cDNAs of the single cells were then pooled together for the following steps. Biotinylated pre-indexed primers were used to further amplify the PCR (95 °C for 3 min, then 4 cycles of: 98 °C for 20 s, 65 °C for 15s, and 72 °C for 5 min, 4 °C hold). Approximately 300 ng cDNA was sheared to approximately 300 bp by Covaris S2, and the 30 terminals of the cDNA was captured by Dynabeads MyOne Streptavidin C1 beads (Thermo Fisher). We constructed a library based on the enriched cDNA fragments, which were attached to the C1 beads, using KAPA Hyper Prep Kits (KK8505). We used the NEB U-shape adaptor for ligation. Libraries were sequenced to generate 150-bp paired-end reads on an Illumina Novaseq 6000 platform.

2.20. Single-cell RNA-seq pre-processing

Raw reads are obtained from well-designed scRNA-seq experiments,

quality control (QC) is performed. Low-quality bases (usually at the 3′end), TSO sequences, polyA sequences and adapter sequences was removed at this pre-processing step. The stripped sequences were then aligned to the mouse (*Mus musculus*) reference genome of mm10 using STAR (version 2.7.9a) (parameters: -soloType CB_UMI_Simple –solo-CBmatchWLtype 1 MM_multi –soloMultiMappers Unique). Seurat (version 4.0.5) [62] was used to normalize and verify expression level of between samples (parameters: default). Raw expression counts are normalized using 'NormalizeData' and 'ScaleData'. The raw data of single-cell RNA-seq are available in the Genome Sequence Archive (GSA) under accession number CRA007296.

2.21. Region segmentation and visualization

Two major clusters were determined by 'FindClusters' function in Seurat with parameters resolution as 0.6, among which SO-MII and MCO-MII were clustered into the same cluster. UMAP was used to visualize the single-cell analysis results.

We selected 2424 marker genes according to published data [63,64], and defined the group gene expression value E_Cˆg as:

$$E_C^g = \frac{1}{N_C} \sum_{cell\ c\ in\ C} E_C^g$$

where E_cˆg represents cell gene expression within one group, and Nc represents numbers of cell in group C. We then calculated the Pearson correlation coefficient and visualized the result in heatmap.

2.22. Identification of the differentially expressed genes

Within each group in SO-MII, MCO-MII, and GV, we utilized the 'FindAllMarkers' function in Seurat package with parameters logfc. threshold = 1 and min. pct = 0.25 to identify differentially expressed genes.

We used Resampling methods to test the overlap of differentially expressed genes within one group. In SO-MII or MCO-MII samples, we resampled 50X times. In each run, we took 20 cells and divided evenly into two categories C_1 and C_2. We next utilized 'FindAllMarkers' function to accordingly identify the differentially expressed genes of C_1 and GV as well as C_2 and GV, selecting top 1000 upregulated and top 1000 downregulated differentially expressed genes of the two comparisons, marked as G_1 and G_2. We then calculated the number N_i of overlap genes between G_1 and G_2, and finally obtained the mean overlap value by:

$$N = \frac{1}{50} \sum_{i=1}^{50} N_i$$

where i represents each run in resampling process.

2.23. Pathway enrichment analysis

We utilized the 'enrichGO' and 'enrichKEGG' functions in the clusterProfiler package to analysis pathway enrichment of differentially expressed genes, where parameters were set as pvalueCutoff = 0.05, qvalueCutoff = 0.05. Results were visualized by heatmap, barplot, and circos plot.

To estimate the variation of pathway activity over each sample population on the KEGG and Hallmarks pathway dataset, we utilized the 'gsva' function in the gsva package to analyze gene set variation analysis.

2.24. Putative chromosome ploidy analysis

For CNV analysis, we leverage the R package scCancer developed by Gu Lab [65]. The function 'runMalignancy' was used, while diploid mouse cells were set as a reference. Results were visualized by the UMAP plot.

2.25. Protein networks analysis

The protein networks analysis was performed by the STRING online website (Version 11.5) with a cutoff of 0.15.

2.26. DCFH-DA dye staining

The ROS level was detected by DCFH-DA dye according to its instruction. The follicle was incubated with 10 μm DCFH-DA in HBSS for 30 min. Then the dye was washed with HBSS. The nuclear was stained with 1 μm Hochest 33342 and visualized by A1 HD25 confocal. The Hochest intensity difference between the experimental and control groups corrected the fluorescence intensity of DCFH-DA.

3. Results

3.1. Follicular growth occurred in the SOCS mimicking a similar mechanical modulus with mouse ovary

To develop the SOCS, we derived sacrificial microspheres of gelatin using a microfluidic chip. Most volumes of microspheres were buried into GelMA and dissolved in a warm medium. Then, the semi-opened culture cavity was exposed and waiting for follicle implantation (Fig. 1a). Previous studies reported the follicle might behave differently in the same hydrogel with different concentrations. Therefore, we questioned whether a similar phenomenon would be observed in the SOCS. The concentration and degree of substitution of methacryloyl of GelMA will dramatically affect its mechanical strength. Thus, we divided the GelMA samples into six groups: the concentration was 5%, 10%, and 15% associated with the substitution of the degree of 60% methacryloyl (GelMA 60, G60) and 90% methacryloyl (GelMA 90, G90). To evaluate GelMA conditions, we created microspheres larger than mouse-developing follicles to exclude the size limitation. Preantral follicles with one or two layers of granulosa cells were implanted, and their sizes increased in 10% and 15% conditions but not in 5% conditions (Fig. 2a–b). The statistical analysis of follicle sizes and live/death ratio showed that follicles cultured in either 5% - G60 or 5% - G90 conditions had smaller sizes but a higher death rate than those cultured in 10% or 15% conditions (Fig. 2c–d). Although there was no significant difference in follicle sizes among 10% - G60, 10% - G90, 15% - G60, and 15% - G90 (Fig. 2c), the 10% - G90 condition was better than others since the percentage of large follicles (>300 μm diameters) was mildly higher while the death rate was slightly lower than other conditions after ten days culture (Fig. 2d).

Next, we questioned why the 10% or 15% condition supports follicular growth. The elastic modulus of the ovary (the indentation points >80) and GelMA (the indentation points >100) was obtained by atomic force microscope (AFM) indentation. By fitting the curve to the distribution of indented elastic modulus, the result revealed the elastic modulus peak of the ovary located between 10% - G60 and 15% - G60 in Fig. 2e, or between 10% - G90 and 15% - G90 in Fig. 2f. The individual fitting curve is represented in Fig. S2. Meanwhile, the average modulus of the ovary was 1.511 ± 0.357 kPa, which is also located between 10% - G60 (0.253 ± 0.128 kPa) and 15% - G60 (2.62 ± 0.766 kPa) or between 10% - G90 (0.904 ± 0.155 kPa) and 15% - G90 (1.91 ± 0.041 kPa) (Fig. S3a). The result indicated that 10% or 15% of GelMA mimicked the ovarian mechanical modulus, therefore, might be suitable for follicle culture.

To evaluate 10% - G90 condition, a published 3D culture method with alginate [54,55] was set as a control. By statistical analysis, the diameter of follicles in the 10% - G90 condition showed no obviously different with the alginate condition (Figs. S3b and S3c), suggesting 10% - G90 provided a suitable environment for follicular growth. Therefore, according to our data, 10% - G90 was screened out for further fabrication of the MCO to evaluate its biological activities.

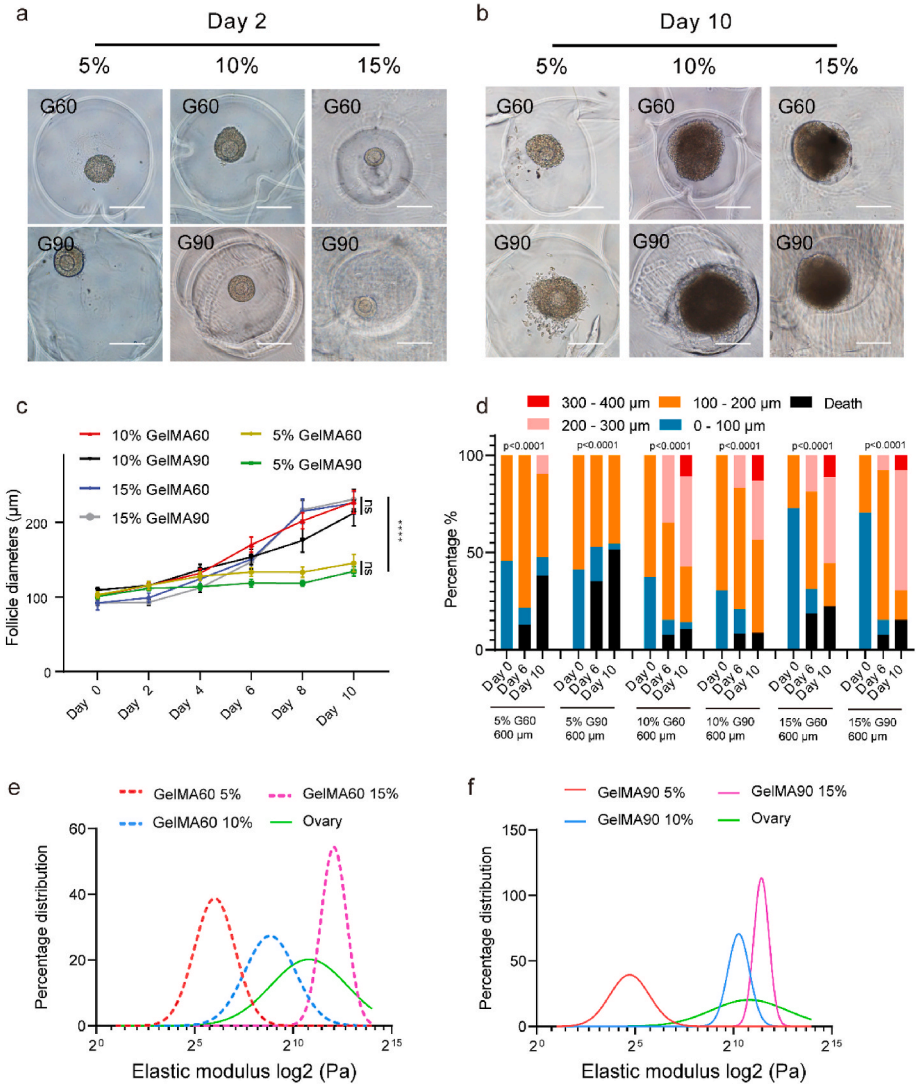

Fig. 2. Optimization of different GelMA conditions for the semi-opened culture system. **a**. The follicle was cultured in different GelMA conditions on day 2. The scale bar was 200 μm. **b**. The follicle was cultured in different GelMA conditions on day 10. The scale bar was 200 μm. **c**. The follicle diameter in 10% and 15% GelMA conditions was larger than that in 5% GelMA, n > 11, the error bar stands for standard error of the mean, the p-value passed two-way ANOVA test, ns: $p > 0.05$; ****: $p < 0.0001$. **d**. The follicle size distribution in different GelMA conditions, the p-value passed the Chi-square test, ****: $p < 0.0001$. **e**. The fitting curve of elastic modulus distribution of mouse ovary and GelMA 60. **f**. The fitting curve of elastic modulus distribution of mouse ovary and GelMA 90.

3.2. The cavity size limited follicular growth and ovulation in the SOCS

The mouse ovarian follicle size ranged from ~100 μm (secondary follicles) to 400–500 μm (antral follicles) [65,66] after activation. The antral cavity occurs when the size is larger than 200 μm, which is essential for oocyte maturation. Therefore, we questioned whether the cavity size of SOCS would limit follicular growth. Herein, we used a T-shape microfluidic chip to produce gelatin microspheres with diameters of 200 μm, 400 μm, and 600 μm (Fig. S4), standing for a small, middle, and large culturing cavity. A non-cavity condition was included to evaluate the follicle behaviors. As a result, granulosa cells dissociated after several days of culture (Fig. S5), indicating the SOCS contributed to maintaining the structure of follicles. The result of follicle growth in cavities revealed that the average size of follicles cultured in 600 μm cavities was larger than those in 200 μm cavities after ten days of culture (Fig. 3a). Interestingly, the ovulation process was only observed in 600 μm cavities at a ratio of 36% (8/22) after the ovulation induction (Fig. 3b). In addition, we found the distribution of sizes was different. All follicles were less than 200 μm when cultured in 200 μm cavities, and the death rate in 200 μm cavities was higher than in others. Large follicles (>300 μm) were only observed in 600 μm cavities (Fig. 3c). These results implied that the growth and ovulation of follicles required a 600 μm culturing cavity that might be owing to less restriction to granulosa cell expansion.

3.3. Fabrication of the MCO scaffold based on the optimized SOCS

The SOCS could be restricted to the shape of the ovarian-mimetic structure by molding approach. To mimic the distribution of follicles in the ovary, the location of follicles was revealed by the Anti-müllerian hormone (Amh) staining. The staining result revealed that the follicle grew beneath the surface in a scattered pattern (Fig. 4a). To build the ovarian-mimetic mold, a convex mold was fabricated through digital Light processing (DLP) 3D printing and used as the template to fabricate the concave PDMS mold. The MCO was derived from the PDMS mold (Fig. 1b). The gelatin microsphere was labeled by red fluorescence and poured into the MCO mold. Then the GelMA was conjugated with green fluorescence and poured into the mold to cover the microsphere. After gelation, the major volume of the sphere was buried into the GelMA (Fig. 4b). Then, the MCO scaffold was finished by dissolving the microsphere (Fig. 4c). The intact adult mouse ovary (Fig. S6a) and the MCO scaffold were scanned by scanning electron microscope (SEM) to evaluate the scaffold. The inside ovarian cavity was exposed and visualized by SEM by tearing off a small piece of the surface epithelium of the ovary (Fig. 4d, Figs. S6b–S6c). As for the MCO scaffold, the semi-opened cavity could be observed, which would then serve as a nest to support follicle growth (Fig. 4e). In addition, the unclosed cavity left an opening for the release of the oocyte once the oocyte matured. To confirm its function, we implanted mouse follicles and tested the

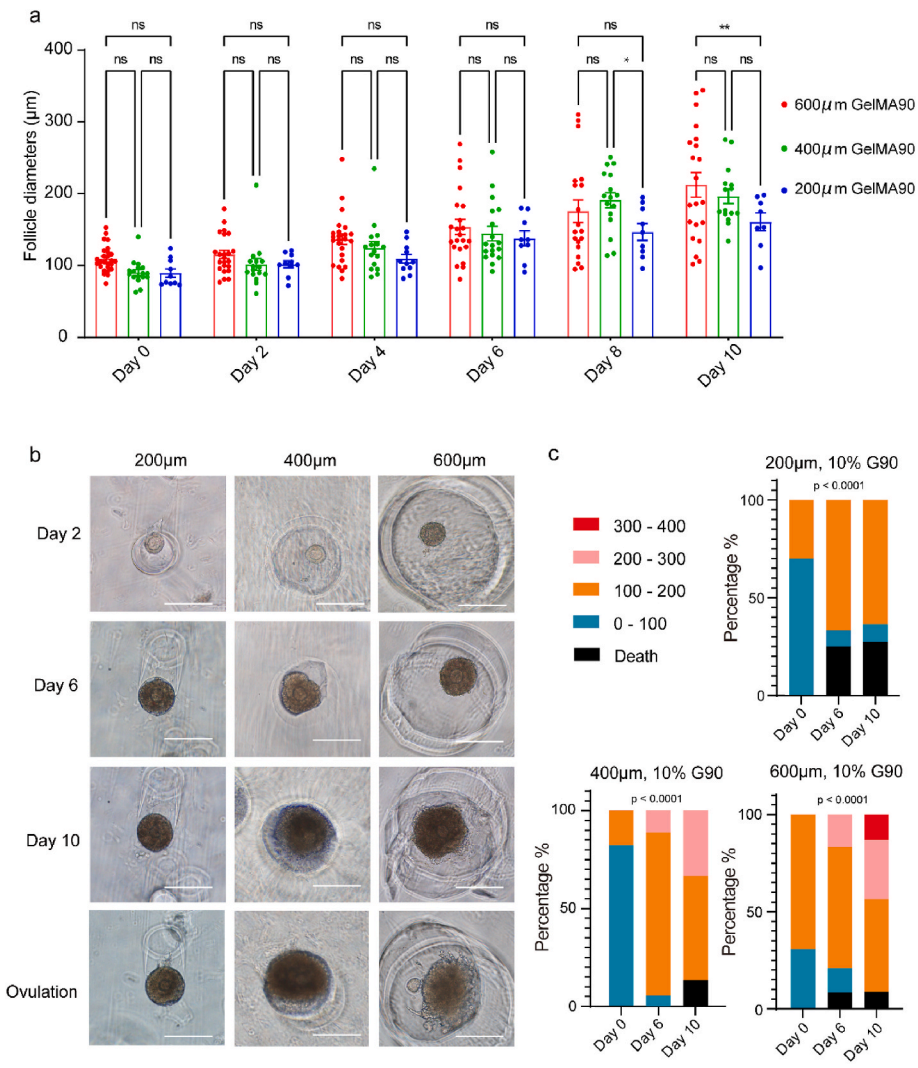

Fig. 3. Optimization of the size of gelatin microspheres for the MCO fabrication. **a**. The statistical summary of follicle diameters cultured in different sizes of cavities, n > 8, the error bar stands for standard error of the mean, the p-value passed two-way ANOVA test, ns: $p > 0.05$; *: $p < 0.05$; **: $p < 0.01$. **b**. Folliclular growth and ovulation in different sizes of cavities created by gelatin microspheres, the bar was 200 μm. **c**. The distribution of follicle diameters cultured in different sizes of cavities, the p-value passed the Chi-square test, ****: $p < 0.0001$.

biological functions of the MCO scaffold.

3.4. Follicular morphology within the semi-opened MCO in vitro

Granulosa cell proliferation within the folliculogenesis will expand the follicle size and develop an antrum filled with follicle fluid. We seeded 20–30 immature follicles into each MCO for *in vitro* culture. The GelMA is enriched with arginine-glycine-aspartic acid (RGD), enabling cell attachment [67,68]. The SEM was used to scan the cavity with follicles to prove the follicle adhering and sprouting inside the cavity rather than in other places (Fig. S7). Then, the increased size and a clear antrum cavity were identified after seven days of culture (Fig. 5a). The histology results represented the three main stages from secondary to antral follicles (Fig. 5b). Next, we questioned whether the marker of granulosa cells and oocytes was normally expressed. Amh and deleted in azoospermia like (Dazl) were stained for they are only expressed in granulosa cells and oocytes, respectively [69,70]. Our staining result showed that Amh and Dazl were expressed separately in granulosa cells and oocytes (Fig. 5c).

3.5. Evaluation of ovarian functions within the semi-opened MCO

Alongside oocyte maturation *in vivo*, female hormones rise and fall in specific patterns [71]. Here, we analyzed the secretion level of estradiol, inhibin-A, and inhibin-B. Estradiol was gradually accumulated at the peak of 36.3 ± 17.0 ng/ml (Fig. 6a) after culture. Specifically, inhibin-A and inhibin-B are produced by dominant and developing follicles, respectively [72,73], which are positively correlated with the estradiol level [74]. Our data revealed an increase of inhibin-A (Fig. 6b) and inhibin-B (Fig. 6c) from day 5, suggesting the activation of follicular growth within the MCO.

Although the precise mechanism of ovulation is still under investigation, this process happens spontaneously *in vivo*. We questioned whether the spontaneous process could be recapitulated within MCO. After triggering the ovulation, MCO was then cultured in a living cell workstation. The dynamic morphology of follicles was recorded per 25 min to monitor the ovulation process. The cumulus expansion was observed first, and then the cumulus-oocyte complex (COC) was released from the cavity opening (Fig. 6d, movie S1). In contrast, the cell proliferation and release were impeded (Fig. S8a, movie S2) if follicles were cultured in alginate, suggesting the semi-opened MCO has advantages in mimicking the dynamic ovarian process. The ovulation rate was 40.9% ± 14.3% within the MCO, which showed no significant difference with the alginate culture model (Fig. S8b). The released COC floated in the medium (Fig. S8c) was collected for in-depth analysis.

Additionally, the extruded oocyte was collected to examine the competence of meiosis. The polar body and the spindle structure were identified, indicating that the fully matured MII oocyte has been ovulated (Fig. 6e). To expand the potential application of the MCO, we questioned whether the ovulated oocyte was fertile. Spontaneous

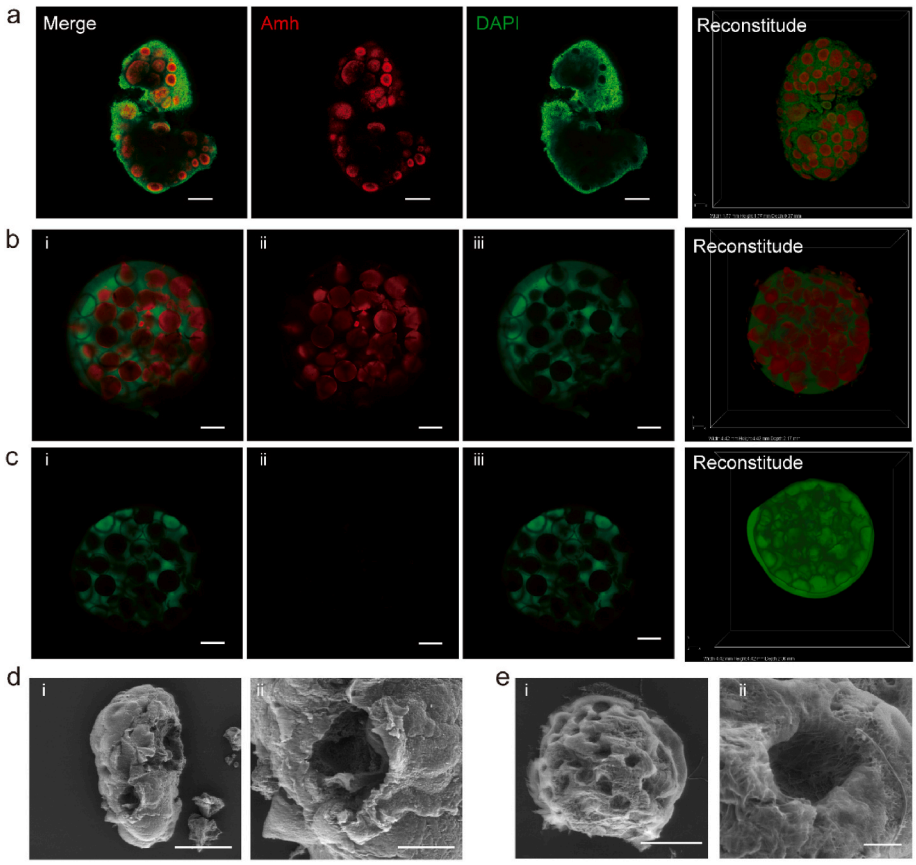

Fig. 4. Fabrication of the semi-opened MCO scaffold. **a**. Amh antibodies identified the physiological structure of mouse ovary follicles. The scale bar was 200 μm. **b**. The structure of the MCO scaffold with gelatin microspheres, the scale bar was 500 μm. **c**. The structure of the MCO scaffold after the dissolution of gelatin microspheres, the bar was 500 μm. **d**. The SEM image of a mouse ovary by tearing off a piece of the surface epithelium, the scale bar was 500 μm (left panel) and 100 μm (right panel). **e**. The SEM image of the MCO scaffold after the dissolution of gelatin microspheres, the scale bar was 1 mm (left panel) and 100 μm (right panel).

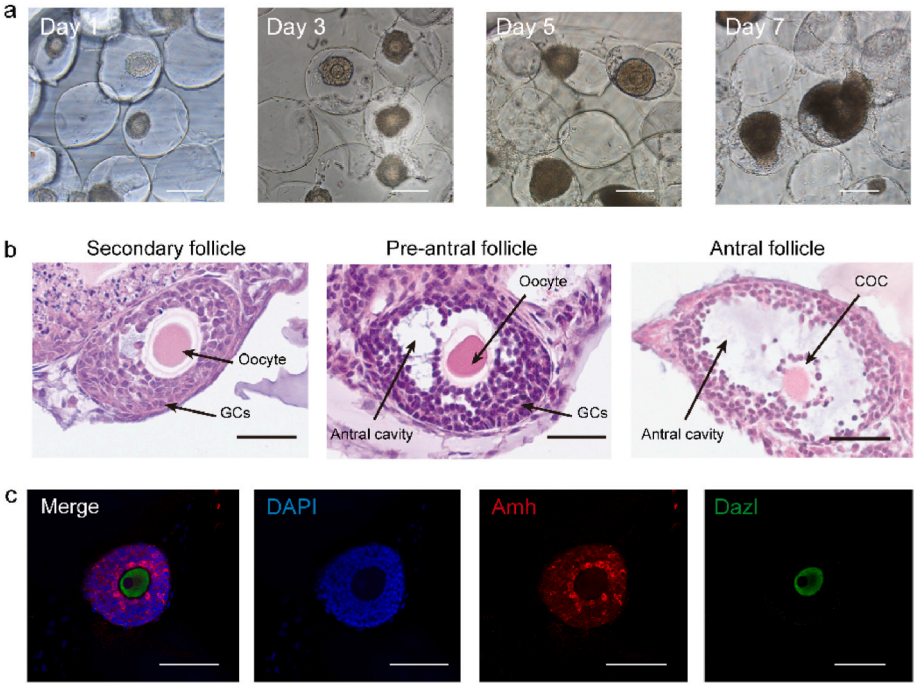

Fig. 5. Characterization of the follicular morphology within the semi-opened MCO. **a**. The follicle increased their sizes within the MCO from day 1 to day 7. The scale bar was 200 μm. **b**. The H&E histological analysis of folliculogenesis from the secondary follicle to the antral follicle. GCs: granulosa cells; COC: cumulus-oocyte complex, the scale bar was 50 μm. **c**. Amh and Dazl were expressed by granulosa cells and the oocyte, respectively. The scale bar was 100 μm.

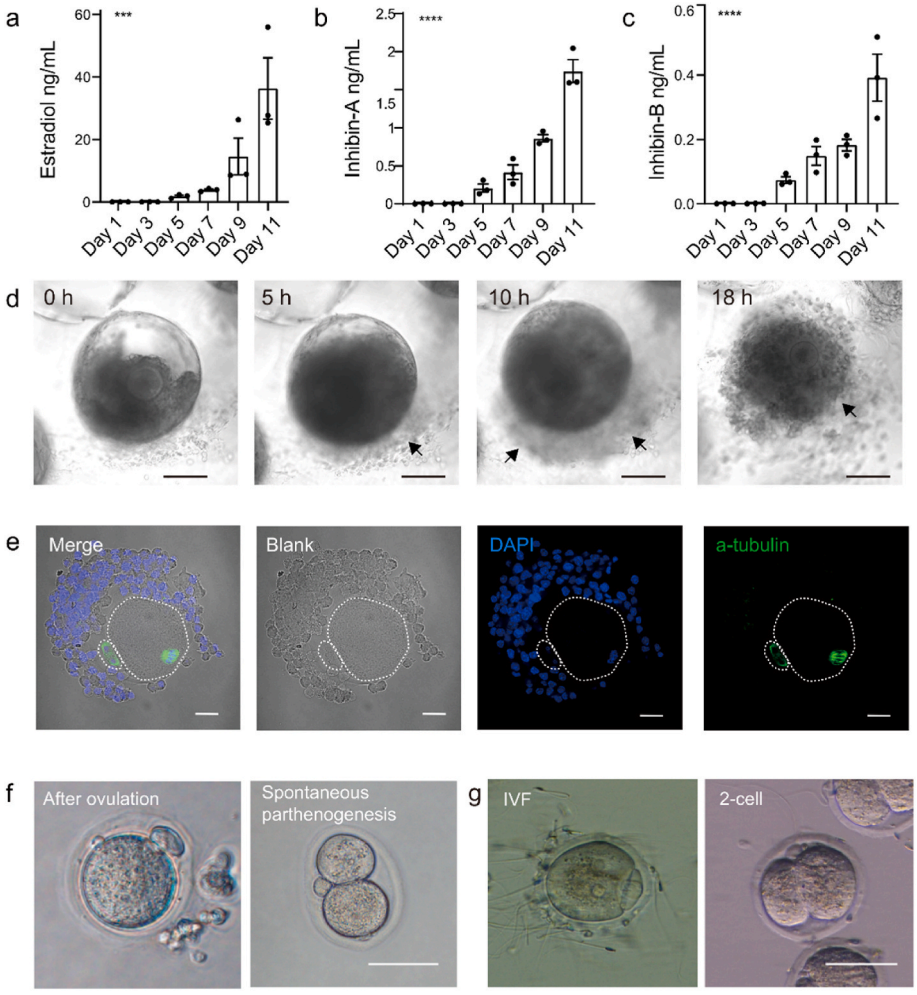

Fig. 6. Characterization of the ovarian process within the MCO. **a – c**. Female hormones: mouse estradiol, mouse Inhibin-A, and mouse Inhibitin-B were expressed within the MCO, n = 3, 20–30 follicles were implanted in the MCO, the error bar stands for standard error of the mean, and the p-value passed the one-way ANOVA test, ***: $p < 0.001$; ****: $p < 0.0001$. **d**. In the time-lapse record of the entire ovulation process, the black arrow indicates the released cells. The bar was 100 μm. **e**. The ovulated oocyte was in the meiosis matured stage. The scale bar was 20 μm. **f**. The spontaneous parthenogenesis of the ovulated oocyte. The scale bar was 50 μm. **g**. The ovulated oocyte developed to the 2-cell stage after IVF. The scale bar was 50 μm.

parthenogenesis occurred in a prolonged culture with hCG and mEGF (Fig. 6f). More directly, IVF was performed. The result revealed that the ovulated oocyte started to cleave into a 2-cell stage around 12h after the end of IVF (Fig. 6g) in a ratio of 25.6% (10/39).

3.6. *The transcriptome of the MCO-MII oocytes was similar to the in vivo MII oocytes*

To characterize the ovulated oocytes from the MCO, we sequenced 22 single MII oocytes from the MCO, 30 single MII oocytes from the super-ovulated mouse and 30 germinal vesicle (GV) oocytes from the P16 mouse before transplantation to the biomimetic ovary. After stringent filtering, 21 MCO-MII oocytes, 30 super-ovulated MII (SO-MII) oocytes, and 30 GV oocytes were retained for further analysis. On average, 8812 genes, 8516 genes, and 12370 genes were identified from MCO-MII, SO-MII, and GV oocytes, as shown in Fig. S9a. Oocyte samples from different mice were mixed well and showed no batch effect in the uniform manifold approximation and projection (UMAP) plot (Fig. S9b). Unique molecular identifier (UMI) transcripts were examined in each sample, showing no apparent differences among the same group (Fig. S9c). We also examined the expression of mitochondrion genes to exclude contamination (Fig. S9d). These data suggested that the sequencing result was of great quality for further analysis.

Two clusters were identified in the UMAP plot. In this plot, MCO-MII oocytes and SO-MII oocytes were divided as cluster 1, while GV oocyte was divided as cluster 2 (Fig. 7a). Markers of ectoderm, mesoderm, endoderm, and germ cells were examined to confirm the samples expressing oocyte markers, as shown in the feature plot (Fig. S9e). Early folliculogenesis genes, such as *Nobox* and *Tnni3*, were maintained at a higher level in GV oocytes (Fig. S9f), whereas early embryo development-related genes were higher in MCO-MII and SO-MII oocytes (Fig. S9g). Some variably expressed genes were identified when comparing MCO-MII and SO-MII oocytes (Fig. S10a). Among them, apoptosis inhibition marker *Xaf1,* whereas mechanoresponsive gene *Yap1* might serve as the center factors (Figs. S10b–S10d), causing the difference in oocytes between *in vivo* and *in vitro*.

Next, the Pearson correlation was performed to evaluate the similarity among GV, SO-MII, and MCO-MII oocytes (Fig. 7b). The result revealed that the correlation between SO-MII and MCO-MII oocytes was 0.97, higher than that of SO-MII versus GV (correlation was 0.72) and MCO-MII versus GV (correlation was 0.74). This result indicated a high similarity between SO-MII and MCO-MII oocytes. Furthermore, the putative chromosome ploidy (PCP) value was evaluated. The MCO-MII oocytes showed the same chromosome ploidy compared to the SO-MII oocyte. In contrast, the GV oocyte showed the ploidy was double (Fig. 7c), supporting MCO-MII oocytes finishing the first cleavage of meiosis, as shown in Fig. 6e. Moreover, for a particular oocyte stage, if some of the MCO-MII oocyte's differential expressed genes (DEGs) and SO-MII oocyte's DEGs participated in the same biological process, these shared genes and biological processes would provide valuable information to evaluate the similarity between them. Therefore, we performed a scatter plot to show that the DEGs of SO-MII versus MCO-MII oocytes (Fig. 7d) were less than that of DEGs obtained from SO-MII versus GV oocytes (Fig. 7e) or MCO-MII versus GV oocytes (Fig. 7f). Furthermore, a Heatmap based on DEGs of SO-MII versus GV (Fig. 7g, Table S1) or MCO-MII versus GV (Fig. 7h, Table S2) indicated MCO-MII

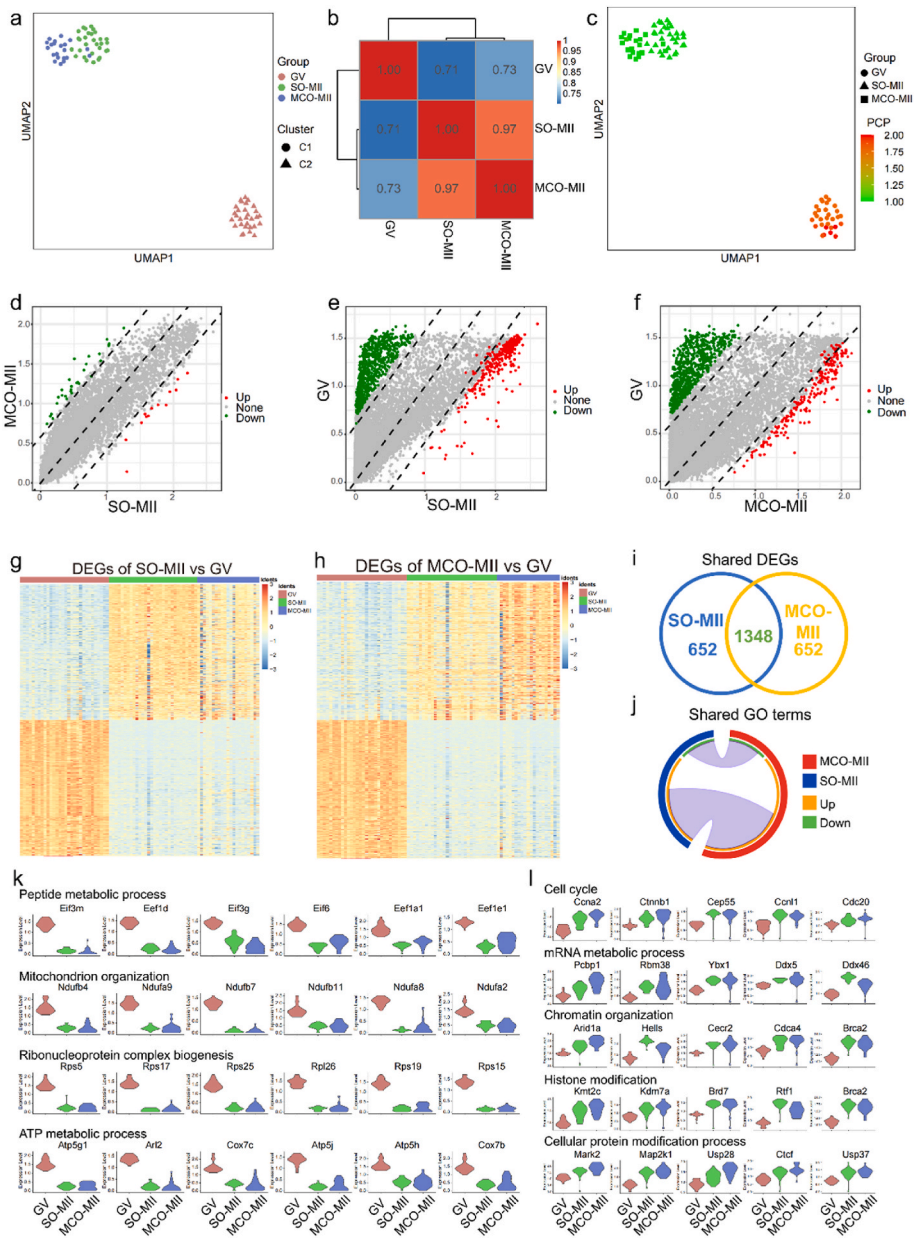

Fig. 7. Single-cell RNA-sequencing of GV, SO-MII, and MCO-MII oocytes. **a**. Cell cluster analysis by UMAP plot. **b**. Pearson correlation analysis of GV, SO-MII, and MCO-MII oocytes. **c**. The putative chromosome ploidy value of GV, SO-MII, and MCO-MII oocytes. **d**. Scatter plot between SO-MII and MCO-MII oocytes. **e**. Scatter plot between GV and SO-MII oocytes. **f**. Scatter plot between GV and MCO-MII oocytes. **g**. Heatmap of DEGs obtained from SO-MII versus GV oocytes. h. Heatmap of DEGs obtained from MCO-MII versus GV oocytes. **i**. VENN map of shared DEGs between SO-MII and MCO-MII oocytes. **j**. Circos plot of shared GO terms between SO-MII and MCO-MII oocytes. **k**. Down-regulated genes in SO-MII and MCO-MII oocytes. **l**. Up-regulated genes in SO-MII and MCO-MII oocytes.

oocytes and SO-MII oocytes shared the major DEGs. In total, 1347 shared DEGs were identified between SO-MII and MCO-MII oocytes (Fig. 7i). To evaluate their similarities, we randomly divided SO-MII or MCO-MII oocytes into 2 groups (10 oocytes each). We obtained the average number of shared DEGs between groups by separately comparing them to GV oocytes for 50X times. Hundreds of DEGs were varied even in the same MII oocyte sample (Figs. S11a and S11b), supporting that 1347 shared DEGs reflecting a strong similarity between SO-MII oocytes and MCO-MII oocytes. Then, we performed gene ontology (GO) and found that over half of GO terms were shared by MCO-MII and SO-MII oocytes (Fig. 7j, Figs. S11c–S11f, Tables S3–S6). In addition, we also performed KEGG and Hallmarks pathway analysis. The result supported the MCO-MII, and SO-MII oocyte enriched similar signaling pathways (Figs. S12 and S13). The shared DEGs between MCO-MII and SO-MII oocytes provided clear clues regarding whether they were in the same developmental stage. We found that genes related to metabolic biological processes were degraded in MCO-MII and SO-MII oocytes (Fig. 7k). On the other hand, genes related to cell cycle and histone modification, etc., were accumulated in SO-MII and MCO-MII oocytes (Fig. 7l). These results indicated that MCO-MII oocytes were quite similar to SO-MII oocytes.

3.7. *Discovering the potential effect of ovarian toxic agents within the MCO model*

A 2D culture system was applied for the toxicity test in the pioneered study [75], but it might investigate more results to trace structural remodeling if a 3D follicular structure was maintained during the toxicity test. Herein, we investigated the potential of MCO to serve as an *in vitro* platform for a chemical test. The reactive oxygen species (ROS) are commonly accumulated in oocytes and are associated with age-related ovarian aging or repeated ovulation [53,76], the effect of ROS and ROS scavengers on follicles is an important research field. Herein, we individually used H_2O_2 to induce ROS accumulation within 2D, MCO, and 3D systems. Then, the ROS level was detected by dichloro-dihydro-fluorescein diacetate (DCFH-DA). We observed that the ROS level increased quickly in 2D and MCO systems within 1h, but we found a relatively low level in the 3D system (Fig. 8a–b). Then, we

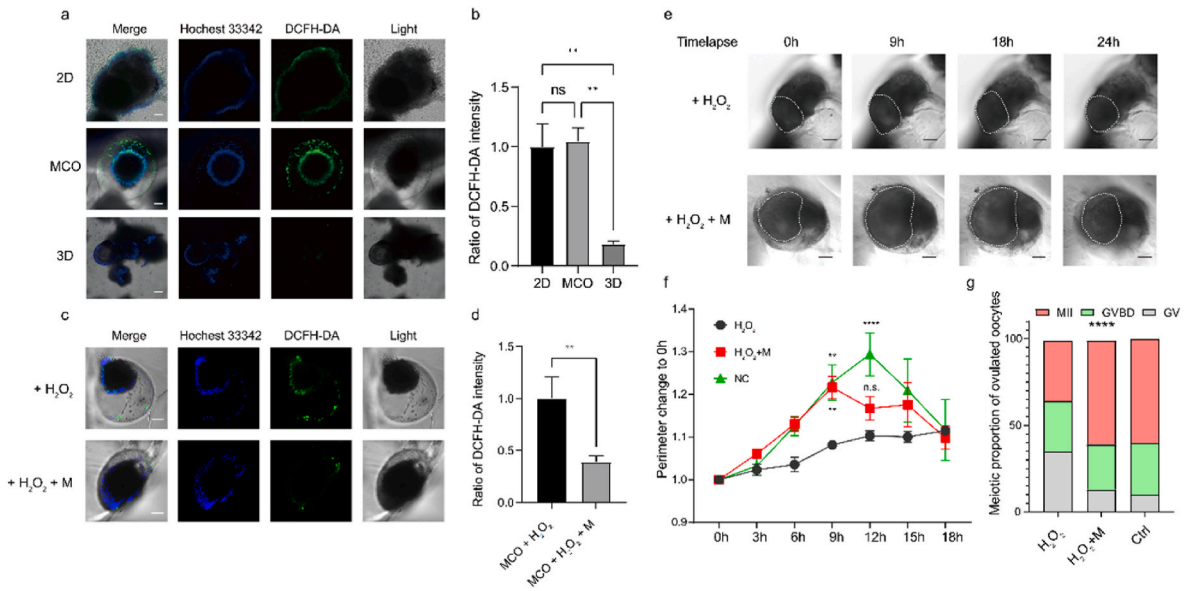

Fig. 8. The MCO is a promising *in vitro* model for chemical test. **a.** The ROS level in 2D, MCO, and 3D culture systems, the scale bar is 100 μm; **b.** The fluorescent intensity of ROS level in 2D, MCO, and 3D culture systems, n > 4; **c.** The ROS level was reduced by melatonin within MCO, the scale bar is 100 μm; **d.** The fluorescent intensity of ROS level within MCO, n > 4; **e.** The time-lapse record of the ovulation process under the treatment of H_2O_2 or H_2O_2 plus melatonin, the scale bar is 100 μm; **f.** The perimeter variation of follicles during the ovulation in H_2O_2 or H_2O_2 plus melatonin condition, 0h was set as basal level, n > 4; **g.** the proportion of GV, GVBD, and MII oocyte in different conditions.

prolonged the incubation time with H_2O_2 till to 24h. The intensity of DCFH-DA was still lower in the 3D system than in 2D and MCO systems (Fig. S14). In previous studies, the intracellular ROS level in germ cells could be reduced by melatonin [77,78]. We investigated whether the MCO could sense the chemical dynamic by subsequent melatonin treatment. The result revealed the ROS level was significantly reduced in the MCO (Fig. 8c–d) and 2D (Fig. S15) models after 4h of melatonin treatment. However, the ROS level in the 3D model was lower than the minimum detectable level and showed an undetectable difference (Fig. S16), validating the MCO could rapidly reflect the chemical change to the difference in the surrounding environment.

Pilot studies suggested ROS strongly correlates with anovulation disorder, but the exact effect of ROS on ovulation dynamic is still under investigation. Therefore, we applied the MCO as an *in vitro* model and focused on the oxidative stress effect on structural remodeling during ovulation. Our data show that the high level of ROS impeded the cumulus expansion process and disrupted the COC rupture (Fig. 8e, movie S3 and S4). To recover the damage of H_2O_2, we treated the MCO with melatonin, a ROS scavenger drug, and re-observed the cumulus expansion process during the ovulation; however, it ended the expansion 3h earlier than anticipated (Fig. 8f), suggesting melatonin is not enough for fully erasing the effect of H_2O_2 and new drugs are still waiting for investigation. Lack of cumulus expansion may produce immature oocytes. Then, oocytes released into the medium were counted and scored by their germinal vesicles and the appearance of the polar body (n > 15). The result showed 35% of oocytes were meiosis matured when treated with H_2O_2, and the maturation rate was increased when co-treated with the MCO with H_2O_2 plus melatonin (Fig. 8g). Together with these data, the MCO was reliable *in vitro* model to evaluate the ROS effect. It is reasonable to assume the MCO has the potential for a universal test of the agent's therapy.

4. Discussion

The ovary is the organ that responds to reproductive behaviors. Although current assistant reproductive techniques (ARTs) provide options to bypass some reproductive processes, such as ovulation, a bioengineered ovary is the equivalent replacement of an ovary which should retain all physiological ovarian functions. Previous studies explored different hydrogels for the 3D culture of mouse follicles. However, the challenge of creating load-bearing structures to recapitulate the complex architecture and physiological functions of native organs remains to be investigated. Herein, we established a novel SOCS culture system and SOCS-based MCO model that can recapitulate several essential processes (including follicle growth, ovulation, and hormone secretion) by mimicking the ovarian elastic modulus and supplying a micro-cavity niche. The previous study reported that primordial follicles grow in a mechanically dynamic environment. The rigid stiffness might support follicle architecture and survival, while the softer ECM might allow follicle expansion and development [79]. Therefore, taking the natural mechanical properties of the ovarian microenvironment as the guide to designing the *in vitro* engineered ovaries is essential. It suggests that our SOCS must incorporate the knowledge of follicles and the physical mechanics to recapitulate a realistic tissue model that mimics the *in vivo* mechanical microenvironment. As for our results, the stiffness of the GelMA was significant in supporting follicular growth. Notably, the follicle grew better on the substrate, which had a similar elastic modulus to the mouse ovary (Fig. 2). It might suggest the substrate can affect the physical nature of follicle development. To mimic the growing pattern of follicles as that *in vivo*, a micro-cavity was fabricated by sacrificial microspheres deriving from a microfluidic system. Considering the diameter of follicles will dramatically increase during the development from primary/secondary follicles to antral follicles, the effect of the cavity size was analyzed. The small size of the microcavity wrapped the follicle and disturbed its maturation, while the large cavity size supported the follicle growth and ovulation (Fig. 3). Although mouse follicles could grow in the empty micro-cavity with a larger diameter than itself, it is concerned to fabricate the MCO with human follicles since a human follicle will grow from a micrometer to a millimeter level. Antral human follicles have been successfully obtained with hydrogel culture [80]. Therefore, one possible solution was obtaining the size-controlled and human follicle-contained microgels derived from microfluidic [81]. It is reasonable to speculate the microgel will be replaced by growing follicles and eventually occupy the whole cavity using MCO's molding approach, but the fabrication parameters should be investigated, which is an important future direction and under

research.

Considering one of the ovarian functions is ovulation, the MCO left openings for the release of the oocyte. We successfully observed that the matured oocyte was ruptured through the opening (Fig. 6d, S6a), whereas the follicle was usually isolated by extra mechanical dissociation or enzyme digestion in a 3D encapsulated culture. This method may induce damage to follicles, and the result varies in batches. In this study, we provide a more reliable ovarian model which permits us to recapitulate the structural remodeling of follicles in the natural ovary, expanding our MCO as an *in vitro* platform to study reproductive behaviors.

The quality of the MCO oocyte was characterized by α-tubulin staining, IVF experiment, and single-cell RNA-seq. On the one hand, the MCO oocyte was meiosis-matured that could be fertilized (Fig. 6e and f) and had a similar transcriptome to the *in vivo* MII oocyte (Fig. 7). On the other hand, we investigated the oocytes had differences in the expression of some specific genes, such as tumor suppressor [82,83] *Xaf1* and mechanoresponsive gene [84] *Yap1* (Fig. S10), which indicated the mechanical difference between *in vitro* and *in vivo* culture environment should be further optimized.

Several factors may affect the oocyte quality. It seems that once the oocyte is released from its follicle, its developmental potential will be affected. In the *in vivo* superovulation cycle, the process was triggered by hCG injection, then the oocyte retrieval was planned within a fixed time frame. Cellular and molecular abnormalities will occur in the oocyte, which remained unfertilized in either the oviduct or culture and underwent a time-dependent deterioration in quality [85]. The second factor that may reduce oocyte competence is follicle size. When submitted to IVM, the oocyte in small or medium size of antral follicles may have insufficient time to undergo cytoplasmic maturation [86], reproducing a lower quality oocyte than *in vivo* oocyte. Our data shows that the number of follicles did not fully grow to their maximum size, which may reduce the subsequent fertilization rate of these oocytes. The ovarian mechanics was essential for follicle development. During the follicle development, follicles migrated from the rigid cortex to the soft medulla, suggesting that the hydrogel with a constant modulus may not be the best condition to support a follicle growth cycle. Regarding our data, although we observed the activation of follicular growth, the follicle size remained variant owing to the fixed hydrogel modulus. The transcriptome of oocyte also reflected the effect of hydrogel mechanics, showing *Yap1* was expressed higher in MCO-MII than in SO-MII. These DEGs might cause the difference, reducing the fertilization rate of MCO-MII oocytes. Therefore, the future research direction is recapitulating the dynamic mechanics in the MCO model and increasing the oocyte quality.

The pioneered study gave a clue to use a 2D culture system to predict chemical toxicity [75]. However, the follicular morphology cannot be maintained. Our result proved that the 3D culture system was insensitive to the chemical change, and the MCO system was beneficial in serving as the *in vitro* model for the toxicity test (Fig. 8). Reproductive aging is linked to the cumulative oxidative damage of oocytes [87], and ROS's role in oocyte quality is well-documented [88,89] by culturing COCs, denuded oocytes *in vitro,* or performing superovulation *in vivo*. Pilot studies suggest that ROS might directly cause the deterioration of oocyte membrane lipids or destroy DNA. Still, our study provided evidence to suggest that ROS could affect the oocyte quality through an indirect manner that cumulus expansion was inhibited by H_2O_2. The cumulus expansion happens in pre-ovulating follicles and is essential for oocyte maturation which leads to the decrease of cAMP in oocytes and results in meiosis resumption [90]. Our data further supported that the maturation of oocytes was also reduced under the H_2O_2 condition. Then we used melatonin, the main secretory antioxidant of the pineal gland, to test its powerful protective action. The protective effect of melatonin is comprehensive. Cao et al. suggested that melatonin might reduce the apoptosis of granulosa cells through the JNK-dependent pathway [52]. Lin et al. found melatonin rescued oxidative stress-enhanced ER stress and cellular senescence of granulosa cells [91]. Probably owing to the protection of melatonin, the cumulus expansion was re-observed during ovulation. We also found the cumulus expansion time ended 3h early in the melatonin group, which was rarely reported and suggested that melatonin administration alone is essential but should be improved to rescue the ROS damage. Our result showing the MCO model could precisely reflect the ovarian effect of agents at a finer temporal scale to investigate more encouraging mechanisms. Many anovulation disorder mechanisms were unknown. Therefore, the MCO could be the *in vitro* tool for studying disorder mechanisms by inducing disease models, tracing cell movement, and testing chemical toxicity.

The bioengineered ovary has advantages in recovering female hormone secretions, conceived ability, and avoiding re-implanting malignant cells [92]. There is an increasing demand for a transplantable engineered ovary for *in vivo* grafting in some cancer patients who are unsuitable for grafting frozen/thawed ovarian tissue [93]. We believe that with the development of engineering technologies and an understanding of the biology of the ovary, the function and structure of the *in vitro* ovary model will be gradually improved and eventually used in the deep application of clinics.

5. Conclusion

Taken together with our data, we have developed a novel method of the SOCS for maintaining a 3D-like structure during the follicle culture. Based on SOCS, we built a semi-opened MCO with GelMA inspired by the mouse ovary's physiological modulus and microstructures. The MCO supported follicular growth, increased hormone secretion, and ovulation. The transcriptome of the MCO-ovulated oocyte was highly similar to natural-ovulated oocytes, with a correlation of 0.97. Furthermore, the MCO could quickly reflect the medium's ROS inducer and scavenger effect. Our result supported that, although melatonin recovered the ovulation, the cumulus expansion ended 3h early than the non-treated group, which was rarely reported, indicating the MCO has the potential as an *in vitro* model for discovering new effects of ovarian toxic agents or drugs. We anticipate that the proposed strategy is potentially valuable for wide applications, including drug screening, pharmacological research, and tissue engineering.

Ethics approval and consent to participate

Animal use was performed under a Tsinghua University Institutional Animal Care and Use Committee (IACUC)-approved protocol with the approval number (222) 368.

CRediT authorship contribution statement

Min Ye: Conceptualization, Methodology, Investigation, Data curation, Validation, Visualization, Writing – original draft, Writing – review & editing. **Yiran Shan:** Software, Methodology, Investigation, Data curation, Writing – original draft. **Bingchuan Lu:** Conceptualization, Methodology, Investigation. **Hao Luo:** Methodology, Investigation. **Binhan Li:** Investigation. **Yanmei Zhang:** Conceptualization, Resources, Writing – review & editing. **Zixuan Wang:** Visualization. **Yuzhi Guo:** Resources. **Liliang Ouyang:** Conceptualization, Resources, Writing – review & editing. **Jin Gu:** Software, Data curation, Methodology, Writing – review & editing. **Zhuo Xiong:** Conceptualization, Methodology, Validation, Supervision, Writing – review & editing. **Ting Zhang:** Conceptualization, Methodology, Validation, Supervision, Writing – review & editing, Funding acquisition.

Declaration of competing interest

There are no conflicts of interest to declare.

Acknowledgment

We thank Laboratory Animal Resources Center at Tsinghua University for the support of mice experiments. We thank Jing Zhang at Tsinghua University School of Life Sciences for contributing to the IVF procedure. We thank you for the support of the Center of Biomedical Analysis at Tsinghua University. We thank Dr. Xunsi Qin for sharing the melatonin reagent. This work was supported by the National Key Research and Development Program of China (Grant No. 2018YFA0703004).

Appendix A. Supplementary data

Supplementary data to this article can be found online at https://doi.org/10.1016/j.bioactmat.2023.02.029.

References

[1] C.J. Williams, G.F. Erickson, in: K.R. Feingold, B. Anawalt, A. Boyce, G. Chrousos, W.W. de Herder, K. Dhatariya, K. Dungan, J.M. Hershman, J. Hofland, S. Kalra, G. Kaltsas, C. Koch, P. Kopp, M. Korbonits, C.S. Kovacs, W. Kuohung, B. Laferrere, M. Levy, E.A. McGee, R. McLachlan, J.E. Morley, M. New, J. Purnell, R. Sahay, F. Singer, M.A. Sperling, C.A. Stratakis, D.L. Trence, D.P. Wilson (Eds.), Morphology and Physiology of the Ovary, Endotext, South Dartmouth (MA), 2000.

[2] N. Rimon-Dahari, L. Yerushalmi-Heinemann, L. Alyagor, N. Dekel, Ovarian folliculogenesis, Results Probl. Cell Differ. 58 (2016) 167–190, https://doi.org/10.1007/978-3-319-31973-5_7.

[3] M.A. Edson, A.K. Nagaraja, M.M. Matzuk, The mammalian ovary from genesis to revelation, Endocr. Rev. 30 (6) (2009) 624–712, https://doi.org/10.1210/er.2009-0012.

[4] J.S. Richards, D.L. Russell, R.L. Robker, M. Dajee, T.N. Alliston, Molecular mechanisms of ovulation and luteinization, Mol. Cell. Endocrinol. 145 (1–2) (1998) 47–54, https://doi.org/10.1016/s0303-7207(98)00168-3.

[5] J.S. Richards, S.A. Pangas, The ovary: basic biology and clinical implications, J. Clin. Invest. 120 (4) (2010) 963–972, https://doi.org/10.1172/JCI41350.

[6] N. Taghizabet, S. Bahmanpour, N.Z. Fard, F. Rezaei-Tazangi, A. Hassanpour, E. K. Nejad, F. Aliakbari, F. Dehghani, In vitro growth of the ovarian follicle: taking stock of advances in research, JBRA Assist Reprod 26 (3) (2022) 508–521, https://doi.org/10.5935/1518-0557.20210076.

[7] M. Belli, G. Vigone, V. Merico, C.A. Redi, M. Zuccotti, S. Garagna, Towards a 3D culture of mouse ovarian follicles, Int. J. Dev. Biol. 56 (10–12) (2012) 931–937, https://doi.org/10.1387/ijdb.120175mz.

[8] J.C. Lousse, J. Donnez, Laparoscopic observation of spontaneous human ovulation, Fertil. Steril. 90 (3) (2008) 833–834, https://doi.org/10.1016/j.fertnstert.2007.12.049.

[9] P. Zorlutuna, N. Annabi, G. Camci-Unal, M. Nikkhah, J.M. Cha, J.W. Nichol, A. Manbachi, H.J. Bae, S.C. Chen, A. Khademhosseini, Microfabricated biomaterials for engineering 3D tissues, Adv. Mater. 24 (14) (2012) 1782–1804, https://doi.org/10.1002/adma.201104631.

[10] A.P. McGuigan, D.A. Bruzewicz, A. Glavan, M. Butte, G.M. Whitesides, Cell encapsulation in sub-mm sized gel modules using replica molding, PLoS One 3 (5) (2008), https://doi.org/10.1371/annotation/0a0b70a9-a6e0-4e60-b6bd-8ef894ed22cd.

[11] Y.A. Du, E. Lo, S. Ali, A. Khademhosseini, Directed assembly of cell-laden microgels for fabrication of 3D tissue constructs, P Natl Acad Sci USA 105 (28) (2008) 9522–9527, https://doi.org/10.1073/pnas.0801866105.

[12] N. Bhamare, K. Tardalkar, A. Khadilkar, P. Parulekar, M.G. Joshi, Tissue Engineering of Human Ear Pinna, Cell Tissue Bank, 2022, https://doi.org/10.1007/s10561-022-09991-7.

[13] A. Khademhosseini, G. Eng, J. Yeh, J. Fukuda, J. Blumling, R. Langer, J.A. Burdick, Micromolding of photocrosslinkable hyaluronic acid for cell encapsulation and entrapment, J. Biomed. Mater. Res. 79a (3) (2006) 522–532, https://doi.org/10.1002/jbm.a.30821.

[14] K. Elkhoury, M. Morsink, L. Sanchez-Gonzalez, C. Kahn, A. Tamayol, E. Arab-Tehrany, Biofabrication of natural hydrogels for cardiac, neural, and bone Tissue engineering Applications, Bioact. Mater. 6 (11) (2021) 3904–3923, https://doi.org/10.1016/j.bioactmat.2021.03.040.

[15] M.M. Laronda, A.L. Rutz, S. Xiao, K.A. Whelan, F.E. Duncan, E.W. Roth, T. K. Woodruff, R.N. Shah, A bioprosthetic ovary created using 3D printed microporous scaffolds restores ovarian function in sterilized mice, Nat. Commun. 8 (2017), https://doi.org/10.1038/ncomms15261.

[16] N. Raffel, R. Dittrich, T. Bauerle, L. Seyler, A. Fattahi, I. Hoffmann, A. Leal-Egana, M.W. Beckmann, A.R. Boccaccini, L. Liverani, Novel approach for the assessment of ovarian follicles infiltration in polymeric electrospun patterned scaffolds, PLoS One 14 (4) (2019), e0215985, https://doi.org/10.1371/journal.pone.0215985.

[17] L. Liverani, N. Raffel, A. Fattahi, A. Preis, I. Hoffmann, A.R. Boccaccini, M. W. Beckmann, R. Dittrich, Electrospun patterned porous scaffolds for the support of ovarian follicles growth: a feasibility study, Sci. Rep. 9 (1) (2019) 1150, https://doi.org/10.1038/s41598-018-37640-1.

[18] B.G. Chung, K.H. Lee, A. Khademhosseini, S.H. Lee, Microfluidic fabrication of microengineered hydrogels and their application in tissue engineering, Lab Chip 12 (1) (2012) 45–59, https://doi.org/10.1039/c1lc20859d.

[19] F.B. Finklea, Y. Tian, P. Kerscher, W.J. Seeto, M.E. Ellis, E.A. Lipke, Engineered cardiac tissue microsphere production through direct differentiation of hydrogel-encapsulated human pluripotent stem cells, Biomaterials 274 (2021), https://doi.org/10.1016/j.biomaterials.2021.120818.

[20] D. Rommel, M. Mork, S. Vedaraman, C. Bastard, L.P.B. Guerzoni, Y. Kittel, R. Vinokur, N. Born, T. Haraszti, L. De Laporte, Functionalized microgel rods interlinked into soft macroporous structures for 3D cell culture, Adv. Sci. 9 (10) (2022), https://doi.org/10.1002/advs.202270060.

[21] L.J. Cai, F.K. Bian, H.X. Chen, J.H. Guo, Y.G. Wang, Y.J. Zhao, Anisotropic microparticles from microfluidics, Chem-Us 7 (1) (2021) 93–136, https://doi.org/10.1016/j.chempr.2020.09.023.

[22] A.C. Daly, L. Riley, T. Segura, J.A. Burdick, Hydrogel microparticles for biomedical applications, Nat. Rev. Mater. 5 (1) (2020) 20–43, https://doi.org/10.1038/s41578-019-0148-6.

[23] Y.C. Fang, Y.H. Guo, M.K. Ji, B.H. Li, Y.J. Guo, J.M. Zhu, T. Zhang, Z. Xiong, 3D printing of cell-laden microgel-based biphasic bioink with heterogeneous microenvironment for biomedical applications, Adv. Funct. Mater. 32 (13) (2022), https://doi.org/10.1002/adfm.202109810.

[24] T.T. Lau, L.Q.P. Lee, W. Leong, D.A. Wang, Formation of model hepatocellular aggregates in a hydrogel scaffold using degradable genipin crosslinked gelatin microspheres as cell carriers, Biomed. Mater. 7 (6) (2012), https://doi.org/10.1088/1748-6041/7/6/065003.

[25] W.Y. Leong, C.J. Fan, D.A. Wang, A novel gelatin-based micro-cavitary hydrogel for potential application in delivery of anchorage dependent cells.: a study with vasculogenesis model, Colloids Surf., B 146 (2016) 334–342, https://doi.org/10.1016/j.colsurfb.2016.06.025.

[26] L. Ouyang, J.P. Wojciechowski, J. Tang, Y. Guo, M.M. Stevens, Tunable microgel-templated porogel (MTP) bioink for 3D bioprinting applications, Adv Healthc Mater 11 (8) (2022), e2200027, https://doi.org/10.1002/adhm.202200027.

[27] J.E. Hornick, F.E. Duncan, L.D. Shea, T.K. Woodruff, Isolated primate primordial follicles require a rigid physical environment to survive and grow in vitro, Hum. Reprod. 27 (6) (2012) 1801–1810, https://doi.org/10.1093/humrep/der468.

[28] A. Shikanov, M. Xu, T.K. Woodruff, L.D. Shea, Interpenetrating fibrin-alginate matrices for in vitro ovarian follicle development, Biomaterials 30 (29) (2009) 5476–5485, https://doi.org/10.1016/j.biomaterials.2009.06.054.

[29] E.R. West, M. Xu, T.K. Woodruff, L.D. Shea, Physical properties of alginate hydrogels and their effects on in vitro follicle development, Biomaterials 28 (30) (2007) 4439–4448, https://doi.org/10.1016/j.biomaterials.2007.07.001.

[30] M. Xu, E. West, L.D. Shea, T.K. Woodruff, Identification of a stage-specific permissive in vitro culture environment for follicle growth and oocyte development, Biol. Reprod. 75 (6) (2006) 916–923, https://doi.org/10.1095/biolreprod.106.054833.

[31] G. Nagamatsu, S. Shimamoto, N. Hamazaki, Y. Nishimura, K. Hayashi, Mechanical stress accompanied with nuclear rotation is involved in the dormant state of mouse oocytes, Sci. Adv. 5 (6) (2019), https://doi.org/10.1126/sciadv.aav9960.

[32] J.A. Yoon, K.A. Lee, J.K. Choi, A simplified 3D culture system for ovarian follicles utilizing a solid matrigel drop to create an in vivo-like ovarian microenvironment, Journal of Biomaterials and Tissue Engineering 9 (4) (2019) 558–561, https://doi.org/10.1166/jbt.2019.2018.

[33] J. Vanacker, V. Luyckx, M.M. Dolmans, A. Des Rieux, J. Jaeger, A. Van Langendonckt, J. Donnez, C.A. Amorim, Transplantation of an alginate-matrigel matrix containing isolated ovarian cells: first step in developing a biodegradable scaffold to transplant isolated preantral follicles and ovarian cells, Biomaterials 33 (26) (2012) 6079–6085, https://doi.org/10.1016/j.biomaterials.2012.05.015.

[34] J. Vanacker, V. Luyckx, M.M. Dolmans, A. Des Rieux, J. Jaeger, A. Van Langendonckt, J. Donnez, C.A. Amorim, Transplantation of an alginate-matrigel matrix containing isolated ovarian cells: first step in developing a biodegradable scaffold to transplant isolated preantral follicles and ovarian cells, Biomaterials 33 (26) (2012) 6079–6085, https://doi.org/10.1016/j.biomaterials.2012.05.015.

[35] S. Joo, S.H. Oh, S. Sittadjody, E.C. Opara, J.D. Jackson, S.J. Lee, J.J. Yoo, A. Atala, The effect of collagen hydrogel on 3D culture of ovarian follicles, Biomed. Mater. 11 (6) (2016), https://doi.org/10.1088/1748-6041/11/6/065009.

[36] J. Vanacker, C.A. Amorim, Alginate: a versatile biomaterial to encapsulate isolated ovarian follicles, Ann. Biomed. Eng. 45 (7) (2017) 1633–1649, https://doi.org/10.1007/s10439-017-1816-6.

[37] N. Desai, F. Abdelhafez, A. Calabro, T. Falcone, Three dimensional culture of fresh and vitrified mouse pre-antral follicles in a hyaluronan-based hydrogel: a preliminary investigation of a novel biomaterial for in vitro follicle maturation, Reprod. Biol. Endocrinol. 10 (2012), https://doi.org/10.1186/1477-7827-10-29.

[38] A. Shikanov, R.M. Smith, M. Xu, T.K. Woodruff, L.D. Shea, Hydrogel network design using multifunctional macromers to coordinate tissue maturation in ovarian follicle culture, Biomaterials 32 (10) (2011) 2524–2531, https://doi.org/10.1016/j.biomaterials.2010.12.027.

[39] M.C. Chiti, J. Vanacker, E. Ouni, N. Tatic, A. Viswanath, A. des Rieux, M. M. Dolmans, L.J. White, C.A. Amorim, Ovarian extracellular matrix-based hydrogel for human ovarian follicle survival in vivo: a pilot work, J. Biomed. Mater. Res. B 110 (5) (2022) 1012–1022, https://doi.org/10.1002/jbm.b.34974.

[40] S.E. Pors, M. Ramlose, D. Nikiforov, K. Lundsgaard, J. Cheng, C.Y. Andersen, S. G. Kristensen, Initial steps in reconstruction of the human ovary: survival of pre-antral stage follicles in a decellularized human ovarian scaffold, Hum. Reprod. 34 (8) (2019) 1523–1535, https://doi.org/10.1093/humrep/dez077.

[41] A.E. Jakus, M.M. Laronda, A.S. Rashedi, C.M. Robinson, C. Lee, S.W. Jordan, K. E. Orwig, T.K. Woodruff, R.N. Shah, Tissue papers" from organ-specific

decellularized extracellular matrices, Adv. Funct. Mater. 27 (34) (2017), https://doi.org/10.1002/adfm.201770203.
[42] S. Das, F. Pati, Y.J. Choi, G. Rijal, J.H. Shim, S.W. Kim, A.R. Ray, D.W. Cho, S. Ghosh, Bioprintable, cell-laden silk fibroin-gelatin hydrogel supporting multilineage differentiation of stem cells for fabrication of three-dimensional tissue constructs, Acta Biomater. 11 (2015) 233–246, https://doi.org/10.1016/j.actbio.2014.09.023.
[43] H. Lee, J. Kim, Y. Choi, D.W. Cho, Application of gelatin bioinks and cell-printing technology to enhance cell delivery capability for 3D liver fibrosis-on-a-chip development, ACS Biomater. Sci. Eng. 6 (4) (2020) 2469–2477, https://doi.org/10.1021/acsbiomaterials.9b01735.
[44] S. Xiao, T. Zhao, J. Wang, C. Wang, J. Du, L. Ying, J. Lin, C. Zhang, W. Hu, L. Wang, K. Xu, Gelatin methacrylate (GelMA)-Based hydrogels for cell transplantation: an effective strategy for tissue engineering, Stem Cell Rev Rep 15 (5) (2019) 664–679, https://doi.org/10.1007/s12015-019-09893-4.
[45] R.Z. Lin, Y.C. Chen, R. Moreno-Luna, A. Khademhosseini, J.M. Melero-Martin, Transdermal regulation of vascular network bioengineering using a photopolymerizable methacrylated gelatin hydrogel, Biomaterials 34 (28) (2013) 6785–6796, https://doi.org/10.1016/j.biomaterials.2013.05.060.
[46] P. Kim, A. Yuan, K.H. Nam, A. Jiao, D.H. Kim, Fabrication of poly(ethylene glycol): gelatin methacrylate composite nanostructures with tunable stiffness and degradation for vascular tissue engineering, Biofabrication 6 (2) (2014), https://doi.org/10.1088/1758-5082/6/2/024112.
[47] S.R. Shin, C. Zihlmann, M. Akbari, P. Assawes, L. Cheung, K.Z. Zhang, V. Manoharan, Y.S. Zhang, M. Yuksekkaya, K.T. Wan, M. Nikkhah, M.R. Dokmeci, X.W. Tang, A. Khademhosseini, Reduced graphene oxide-GelMA hybrid hydrogels as scaffolds for cardiac tissue engineering, Small 12 (27) (2016) 3677–3689, https://doi.org/10.1002/smll.201600178.
[48] H. Qi, Y.A. Du, L.Y. Wang, H. Kaji, H.J. Bae, A. Khademhosseini, Patterned differentiation of individual embryoid bodies in spatially organized 3D hybrid microgels, Adv. Mater. 22 (46) (2010) 5276–5281, https://doi.org/10.1002/adma.201002873.
[49] T. Wu, Y.Y. Gao, J. Su, X.N. Tang, Q. Chen, L.W. Ma, J.J. Zhang, J.M. Wu, S. X. Wang, Three-dimensional bioprinting of artificial ovaries by an extrusion-based method using gelatin-methacryloyl bioink, Climacteric 25 (2) (2022) 170–178, https://doi.org/10.1080/13697137.2021.1921726.
[50] Y. Tang, W. Wang, L. Ni, H.C. Liu, A modified protocol for in vitro maturation of mouse oocytes from secondary preantral follicles, Fertil. Steril. 96 (3) (2011), https://doi.org/10.1016/j.fertnstert.2011.07.924. S241-S241.
[51] M. Belli, G. Vigone, V. Merico, C.A. Redi, M. Zuccotti, S. Garagna, Towards a 3D culture of mouse ovarian follicles, Int. J. Dev. Biol. 56 (10–12) (2012) 931–937, https://doi.org/10.1387/ijdb.120175mz.
[52] Y. Cao, M. Shen, Y. Jiang, S.C. Sun, H. Liu, Melatonin reduces oxidative damage in mouse granulosa cells via restraining JNK-dependent autophagy, Reproduction 155 (3) (2018) 307–319, https://doi.org/10.1530/REP-18-0002.
[53] H. Tamura, A. Takasaki, T. Taketani, M. Tanabe, F. Kizuka, L. Lee, I. Tamura, R. Maekawa, H. Aasada, Y. Yamagata, N. Sugino, The role of melatonin as an antioxidant in the follicle, J. Ovarian Res. 5 (2012) 5, https://doi.org/10.1186/1757-2215-5-5.
[54] P. Jamalzaei, M.R. Valojerdi, L. Montazeri, H. Baharvand, Effects of alginate concentration and ovarian cells on in vitro development of mouse preantral follicles: a factorial study, International Journal of Fertility & Sterility 13 (4) (2020) 330–338, https://doi.org/10.22074/ijfs.2020.5746.
[55] E.R. West-Farrell, M. Xu, M.A. Gomberg, Y.H. Chow, T.K. Woodruff, L.D. Shea, The mouse follicle microenvironment regulates antrum formation and steroid production: alterations in gene expression profiles, Biol. Reprod. 80 (3) (2009) 432–439, https://doi.org/10.1095/biolreprod.108.071142.
[56] T.J. Kannanayakal, J. Eberwine, mRNA methods used in dissecting gene expression of the brain, Ageing Res. Rev. 4 (4) (2005) 513–528, https://doi.org/10.1016/j.arr.2005.09.001.
[57] S. Picelli, A.K. Bjorklund, O.R. Faridani, S. Sagasser, G. Winberg, R. Sandberg, Smart-seq2 for sensitive full-length transcriptome profiling in single cells, Nat. Methods 10 (11) (2013) 1096–1098, https://doi.org/10.1038/nmeth.2639.
[58] J.M. Spaethling, M. Sanchez-Alavez, J. Lee, F.C. Xia, H. Dueck, W.S. Wang, S. A. Fisher, J.Y. Sul, P. Seale, J. Kim, T. Bartfai, J. Eberwine, Single-cell transcriptomics and functional target validation of brown adipocytes show their complex roles in metabolic homeostasis, Faseb. J. 30 (1) (2016) 81–92, https://doi.org/10.1096/fj.15-273797.
[59] T. Hashimshony, F. Wagner, N. Sher, I. Yanai, CEL-Seq: single-cell RNA-Seq by multiplexed linear amplification, Cell Rep. 2 (3) (2012) 666–673, https://doi.org/10.1016/j.celrep.2012.08.003.
[60] S. Islam, U. Kjallquist, A. Moliner, P. Zajac, J.B. Fan, P. Lonnerberg, S. Linnarsson, Highly multiplexed and strand-specific single-cell RNA 5' end sequencing, Nat. Protoc. 7 (5) (2012) 813–828, https://doi.org/10.1038/nprot.2012.022.
[61] A.M. Klein, L. Mazutis, I. Akartuna, N. Tallapragada, A. Veres, V. Li, L. Peshkin, D. A. Weitz, M.W. Kirschner, Droplet barcoding for single-cell transcriptomics applied to embryonic stem cells, Cell 161 (5) (2015) 1187–1201, https://doi.org/10.1016/j.cell.2015.04.044.
[62] T. Stuart, A. Butler, P. Hoffman, C. Hafemeister, E. Papalexi, W.M. Mauck, Y. H. Hao, M. Stoeckius, P. Smibert, R. Satija, Comprehensive integration of single-cell data, Cell 177 (7) (2019) 1888, https://doi.org/10.1016/j.cell.2019.05.031.
[63] X.S. Cui, X.Y. Li, X.J. Yin, I.K. Kong, J.J. Kang, N.H. Kim, Maternal gene transcription in mouse oocytes: genes implicated in oocyte maturation and fertilization, J Reprod Develop 53 (2) (2007) 405–418, https://doi.org/10.1262/jrd.18113.
[64] Z.H. Zhao, T.G. Meng, A. Li, H. Schatten, Z.B. Wang, Q.Y. Sun, RNA-Seq transcriptome reveals different molecular responses during human and mouse oocyte maturation and fertilization, BMC Genom. 21 (1) (2020), https://doi.org/10.1186/s12864-020-06885-4.
[65] H.D. Saatcioglu, I. Cuevas, D.H. Castrillon, Control of oocyte reawakening by kit, PLoS Genet. 12 (8) (2016), https://doi.org/10.1371/journal.pgen.1006215.
[66] J. Griffin, B.R. Emery, I. Huang, C.M. Peterson, D.T. Carrell, Comparative analysis of follicle morphology and oocyte diameter in four mammalian species (mouse, hamster, pig, and human), J. Exp. Clin. Assist. Reprod. 3 (2006) 2, https://doi.org/10.1186/1743-1050-3-2.
[67] Y. Liu, M.B. Chan-Park, A biomimetic hydrogel based on methacrylated dextran-graft-lysine and gelatin for 3D smooth muscle cell culture, Biomaterials 31 (6) (2010) 1158–1170, https://doi.org/10.1016/j.biomaterials.2009.10.040.
[68] K. Yue, G. Trujillo-de Santiago, M.M. Alvarez, A. Tamayol, N. Annabi, A. Khademhosseini, Synthesis, properties, and biomedical applications of gelatin methacryloyl (GelMA) hydrogels, Biomaterials 73 (2015) 254–271, https://doi.org/10.1016/j.biomaterials.2015.08.045.
[69] A.G. Grynnerup, A. Lindhard, S. Sorensen, The role of anti-Mullerian hormone in female fertility and infertility - an overview, Acta Obstet. Gynecol. Scand. 91 (11) (2012) 1252–1260, https://doi.org/10.1111/j.1600-0412.2012.01471.x.
[70] M. Brook, J.W. Smith, N.K. Gray, The DAZL and PABP families: RNA-binding proteins with interrelated roles in translational control in oocytes, Reproduction 137 (4) (2009) 595–617, https://doi.org/10.1530/REP-08-0524.
[71] C.K. Welt, Y.L. Pagan, P.C. Smith, K.B. Rado, J.E. Hall, Control of follicle-stimulating hormone by estradiol and the inhibins: critical role of estradiol at the hypothalamus during the luteal-follicular transition, J. Clin. Endocrinol. Metab. 88 (4) (2003) 1766–1771, https://doi.org/10.1210/jc.2002-021516.
[72] N.P. Groome, P.J. Illingworth, M. Obrien, R. Pai, F.E. Rodger, J.P. Mather, A. S. McNeilly, Measurement of dimeric inhibin B throughout the human menstrual cycle, J. Clin. Endocrinol. Metab. 81 (4) (1996) 1401–1405, https://doi.org/10.1210/jcem.81.4.8636341.
[73] C.K. Welt, Z.A. Smith, D.K. Pauler, J.E. Hall, Differential regulation of inhibin A and inhibin B by luteinizing hormone, follicle-stimulating hormone, and stage of follicle development, J. Clin. Endocrinol. Metab. 86 (6) (2001) 2531–2537, https://doi.org/10.1210/jcem.86.6.7597.
[74] C.Y. Andersen, A.G. Byskov, Estradiol and regulation of anti-Mullerian hormone, inhibin-A, and inhibin-B secretion: analysis of small antral and preovulatory human follicles' fluid, J. Clin. Endocrinol. Metab. 91 (10) (2006) 4064–4069, https://doi.org/10.1210/jc.2006-1066.
[75] T. Zhang, Y. Chen, Y. Yang, Z. Wang, Q. Pan, S. Xu, Z. Sun, The potentiality of two-dimensional preantral follicle culture as an in vitro model in predicting premature ovarian failure, Exp. Toxicol. Pathol. 69 (7) (2017) 477–484, https://doi.org/10.1016/j.etp.2017.04.010.
[76] L. Wang, J. Tang, L. Wang, F. Tan, H. Song, J. Zhou, F. Li, Oxidative stress in oocyte aging and female reproduction, J. Cell. Physiol. 236 (12) (2021) 7966–7983, https://doi.org/10.1002/jcp.30468.
[77] X. Zhang, Q. Xia, R. Wei, H. Song, J. Mi, Z. Lin, Y. Yang, Z. Sun, K. Zou, Melatonin protects spermatogonia from the stress of chemotherapy and oxidation via eliminating reactive oxidative species, Free Radic. Biol. Med. 137 (2019) 74–86, https://doi.org/10.1016/j.freeradbiomed.2019.04.009.
[78] Y.F. Wang, X.F. Sun, Z.L. Han, L. Li, W. Ge, Y. Zhao, M. De Felici, W. Shen, S. F. Cheng, Protective effects of melatonin against nicotine-induced disorder of mouse early folliculogenesis, Aging (Albany NY) 10 (3) (2018) 463–480, https://doi.org/10.18632/aging.101405.
[79] E. Ouni, C. Bouzin, M.M. Dolmans, E. Marbaix, S. Pyr Dit Ruys, D. Vertommen, C. A. Amorim, Spatiotemporal changes in mechanical matrisome components of the human ovary from prepuberty to menopause, Hum. Reprod. 35 (6) (2020) 1391–1410, https://doi.org/10.1093/humrep/deaa100.
[80] H. Yin, S.G. Kristensen, H. Jiang, A. Rasmussen, C.Y. Andersen, Survival and growth of isolated pre-antral follicles from human ovarian medulla tissue during long-term 3D culture, Hum. Reprod. 31 (7) (2016) 1531–1539, https://doi.org/10.1093/humrep/dew049.
[81] X. He, Microfluidic encapsulation of ovarian follicles for 3D culture, Ann. Biomed. Eng. 45 (7) (2017) 1676–1684, https://doi.org/10.1007/s10439-017-1823-7.
[82] S.I. Jeong, J.W. Kim, K.P. Ko, B.K. Ryu, M.G. Lee, H.J. Kim, S.G. Chi, XAF1 forms a positive feedback loop with IRF-1 to drive apoptotic stress response and suppress tumorigenesis, Cell Death Dis. 9 (8) (2018) 806, https://doi.org/10.1038/s41419-018-0867-4.
[83] L.M. Zhu, D.M. Shi, Q. Dai, X.J. Cheng, W.Y. Yao, P.H. Sun, Y. Ding, M.M. Qiao, Y. L. Wu, S.H. Jiang, S.P. Tu, Tumor suppressor XAF1 induces apoptosis, inhibits angiogenesis and inhibits tumor growth in hepatocellular carcinoma, Oncotarget 5 (14) (2014) 5403–5415, https://doi.org/10.18632/oncotarget.2114.
[84] G. Nardone, J. Oliver-De La Cruz, J. Vrbsky, C. Martini, J. Pribyl, P. Skladal, M. Pesl, G. Caluori, S. Pagliari, F. Martino, Z. Maceckova, M. Hajduch, A. Sanz-Garcia, N.M. Pugno, G.B. Stokin, G. Forte, YAP regulates cell mechanics by controlling focal adhesion assembly, Nat. Commun. 8 (2017), 15321, https://doi.org/10.1038/ncomms15321.
[85] Y.L. Miao, K. Kikuchi, Q.Y. Sun, H. Schatten, Oocyte aging: cellular and molecular changes, developmental potential and reversal possibility, Hum. Reprod. Update 15 (5) (2009) 573–585, https://doi.org/10.1093/humupd/dmp014.
[86] P. Lonergan, T. Fair, Maturation of oocytes in vitro, Annu Rev Anim Biosci 4 (2016) 255–268, https://doi.org/10.1146/annurev-animal-022114-110822.
[87] H. Sasaki, T. Hamatani, S. Kamijo, M. Iwai, M. Kobanawa, S. Ogawa, K. Miyado, M. Tanaka, Impact of oxidative stress on age-associated decline in oocyte developmental competence, Front. Endocrinol. 10 (2019) 811, https://doi.org/10.3389/fendo.2019.00811.

[88] S.I. Rakha, M.A. Elmetwally, H. El-Sheikh Ali, A. Balboula, A.M. Mahmoud, S. M. Zaabel, Importance of antioxidant supplementation during in vitro maturation of mammalian oocytes, Vet Sci 9 (8) (2022), https://doi.org/10.3390/vetsci9080439.

[89] R.J. Aitken, Impact of oxidative stress on male and female germ cells: implications for fertility, Reproduction 159 (4) (2020) R189–R201, https://doi.org/10.1530/REP-19-0452.

[90] B. Turathum, E.M. Gao, R.C. Chian, The function of cumulus cells in oocyte growth and maturation and in subsequent ovulation and fertilization, Cells 10 (9) (2021), https://doi.org/10.3390/cells10092292.

[91] X. Lin, Y. Dai, X. Tong, W. Xu, Q. Huang, X. Jin, C. Li, F. Zhou, H. Zhou, X. Lin, D. Huang, S. Zhang, Excessive oxidative stress in cumulus granulosa cells induced cell senescence contributes to endometriosis-associated infertility, Redox Biol. 30 (2020), 101431, https://doi.org/10.1016/j.redox.2020.101431.

[92] M.M. Dolmans, V. Luyckx, J. Donnez, C.Y. Andersen, T. Greve, Risk of transferring malignant cells with transplanted frozen-thawed ovarian tissue, Fertil. Steril. 99 (6) (2013) 1514–1522, https://doi.org/10.1016/j.fertnstert.2013.03.027.

[93] M.M. Dolmans, C.A. Amorim, Fertility preservation: construction and use of artificial ovaries, Reproduction 158 (5) (2019) F15–F25, https://doi.org/10.1530/REP-18-0536.